remote sensing

MDPI

Article

Collocated W-Band Radar and Lidar Observations of Taklimakan Dust: Sensitivity to Giant Particles and Contamination by Biological Scatterers

Haoran Si [1], Jicheng Luo [2,*], Minzhong Wang [1], Hu Ming [3], Congzhen Zhu [1], Jiajun Li [4], Jiantao Zhang [1] and Rongyi Chen [1]

[1] Institute of Desert Meteorology, China Meteorological Administration/National Observation and Research Station of Desert Meteorology, Taklimakan Desert of Xinjiang/Taklimakan Desert Meteorology Field Experiment Station of China Meteorological Administration/Xinjiang Key Laboratory of Desert Meteorology and Sandstorm/Key Laboratory of Tree-Ring Physical and Chemical Research, China Meteorological Administration, Urumqi 830002, China; sihr@idm.cn (H.S.); wangmz@idm.cn (M.W.)
[2] Chengdu Yuanwang Technology Co., Ltd., Chengdu 610213, China
[3] School of Electrical and Electronic Engineering, Shandong University of Technology, Zibo 255000, China
[4] School of Computer Science and Technology, Xinjiang University, Urumqi 830046, China
* Correspondence: luojicheng@cdyw.com

Highlights

What are the main findings?

- In heavy dust, only 4.7% of the cells at 0.30–0.99 km were detected by the W-band radar alone, and above 1 km, where the lidar product had no valid data, the radar detected echo in only 1.7% of the cells outside hydrometeor-compatible environments.
- In clear warm air, frequent low-level radar echoes were most likely biological; in a cold dust storm, particles larger than 32 μm produced more than 94% of the dust echo, and those larger than about 50 μm produced most of it.

What are the implications of the main findings?

- W-band reflectivity–PM_{10} relations depend on the giant-particle fraction, which PM_{10} and lidar backscatter do not constrain and optical particle counters do not size.
- Before radar and lidar records are combined in dust studies, warm-season radar records should be screened for biological echoes and the quality-control rules that truncate archived lidar profiles should be checked.

Abstract

W-band radars are expected to detect dust where lidar signals are extinguished. We tested this at Tazhong, Taklimakan Desert, using 2082 collocated 10-min windows of radar, lidar, particle-counter and surface observations from 15 spring days in 2025. At visibility below 0.5 km, the radar alone detected only 4.7% of the 30-m cells at 0.30–0.99 km, depending on the lidar threshold; above 1 km, where the lidar product had no valid data, it detected echo in 1.7% of the cells up to 1.5 km outside hydrometeor-compatible environments. In clear warm air, low-level echoes occurred in 91% of afternoon minutes, with lidar backscatter only 9% above echo-free values. Because these echoes persisted after sunset in calm air and descended far more slowly than giant grains fall, they were most likely biological. Doppler moments could not separate them from warm-season dust echoes. In a cold storm, the counter's 0.25–32-μm particles produced 27 dB less reflectivity than the observed −29.1 dBZ, whereas tower size distributions produced 3.4–10.2 dB more. Particles larger than 32 μm produced over 94% of the echo, and those larger than about 50 μm at least 81% under nominal calibration. The radar added little coverage but strong sensitivity to giant particles; warm-season records must first be screened for biological echoes.

Check for updates

Academic Editor: Tamas Várnai

Received: 23 October 2026
Revised: 17 November 2026
Accepted: 23 November 2026
Published: 27 November 2026

Copyright: © 2026 by the authors. Licensee MDPI, Basel, Switzerland. This article is an open access article distributed under the terms and conditions of the Creative Commons Attribution (CC BY) license.

Keywords: mineral dust; W-band radar; lidar; giant particles; biological echoes; reflectivity closure; Taklimakan Desert

1. Introduction

The Taklimakan Desert is a major source of Asian dust. Dust emitted there is mixed through a convective boundary layer several kilometres deep and then transported downstream [1–3]. The Tazhong station, in the centre of the desert, is part of a long-running observation network [4]. Coarse dust, including giant particles larger than 62.5 μm [5], is common both near and far from sources. It controls dust deposition and contributes to radiative effects, yet models and routine measurements systematically underestimate it [6–10]. Giant particles are lifted in dense dust near the surface, which is also where most profiling instruments perform worst.

Polarisation lidar is the standard instrument for profiling dust. Its depolarisation ratio identifies non-spherical particles, and backscatter at several wavelengths constrains particle size [11–13]. Over the Taklimakan, lidars have documented dust layers several kilometres deep [14–18]. In dense dust, however, lidar has two limitations. First, the signal is extinguished within the lowest kilometre. Second, backscatter is weighted by particle cross-section, so it is insensitive to giant particles, which are few in number. In addition, depolarisation ratios require calibration of the lidar channels [19]. Millimetre-wave radars are expected to overcome both limitations.

In the Rayleigh regime, radar reflectivity is proportional to the sixth power of particle diameter and is therefore dominated by the largest particles. Millimetre-wave signals are also little affected by extinction [20,21]. At Tazhong, wind-profiler, Ka-band and W-band radars have recorded dust echoes, and reflectivity–mass relations have been derived by calibrating reflectivity against PM_{10} [22–26]. Elsewhere, cloud radars have detected giant aerosol particles [27–29], and combined radar and lidar data are used to stratify and classify aerosols, including in the EarthCARE products [30–33]. These studies rest on two assumptions that have not been tested in dense dust. The first is that the radar observes dust where the lidar signal is extinguished; the two instruments, however, have not been compared cell by cell under these conditions. The second is that radar echoes can be related to PM_{10}, although PM_{10} covers only particles smaller than about 10 μm in aerodynamic diameter, whereas reflectivity is dominated by the largest particles. No study has compared the reflectivity observed during a dust storm in a source region with that computed from size distributions that include the giant-particle tail.

Dust is not the only source of low-level radar echoes. Cloud radars record insects and other biological scatterers in the boundary layer, and these echoes follow a diurnal cycle and depend on temperature [34–37]. Cloud-radar studies of giant aerosol therefore have to separate biological echoes from aerosol echoes [29], and millimetre-wave cloud radars in China also record frequent clear-air echoes [38,39]. At Tazhong, a vegetated shelterbelt runs beside the station, and spring afternoon temperatures reach 30 °C. Spring dust episodes can also be accompanied by precipitation echoes aloft. Previous radar dust studies, however, identified dust periods from weather reports and attributed all echoes within these periods to dust. How strongly biological echoes contaminate such records in dense dust near a major source has not been quantified.

Here, we use 15 days of collocated W-band radar, lidar, particle-counter, tower and surface observations at Tazhong in spring 2025 to answer three questions. (1) In dense dust, does the W-band radar detect dust where the lidar does not? (2) Which low-level echoes are not produced by dust, and can they be recognised with single-frequency Doppler moments

and lidar? (3) Which particle sizes produce the radar echo in a dust storm? To answer these questions, we compare radar and lidar detections cell by cell, diagnose the source of clear-air echoes from their dependence on temperature and time after sunset, and compare the observed reflectivity with that computed from measured size distributions that include the giant-particle tail. Section 2 describes the data and methods, Section 3 presents the results, Section 4 discusses their implications and limitations, and Section 5 summarises the conclusions.

2. Materials and Methods

2.1. Site and Instruments

Tazhong station (38.968°N, 83.659°E; about 1100 m above sea level) lies among mobile dunes in the central Taklimakan Desert (Figure 1a,b), with planted trees and a vegetated shelterbelt beside it (Figure 1d). We analyse the 15 days in spring 2025 on which all instruments operated together: 26 March; 3–4, 6 and 8–17 April; and 3 May. These days form five continuous observation blocks containing 144, 288, 144, 1386 and 120 complete 10-min windows (Section 2.2). They also contain seven dust events. To keep the event definition independent from the instruments being compared, we defined the events from surface PM_{10}, $PM_{2.5}$ and wind speed alone, without visibility, lidar or radar data (Text S1).

Table 1 lists the instruments. The vertically pointing W-band Doppler radar (Figure 1c) was built by Chengdu Yuanwang Technology Co., Ltd. (Chengdu, China) and has observed dust at Tazhong since 2024 [26]. It transmits at 94 GHz (wavelength 3.2 mm; 3.206 mm in the data header). According to the manufacturer's data-format documentation, the radar combines pulses of different lengths to cover different ranges. An unmodulated 1-μs pulse covers the range from the edge of its blind zone at 0.15 km, and a linear-frequency-modulated 2-μs pulse, compressed to 15-m resolution, takes over at 0.405 km (gate 27). The 1-μs data are sampled every 15 m, but their range resolution is 150 m. The documentation also lists longer pulses spliced at 1.0 and 2.0 km. However, the processing constant shows no further step out to 5 km (Section 2.3; Table S2a), so only the splice at 0.405 km affects the reflectivity analysed here. The radar recorded the equivalent reflectivity factor Z, mean Doppler velocity V, spectral width W and signal-to-noise ratio (SNR) every 5 s in 15-m gates; we use the gates at 0.15–4.995 km. The archived velocities and widths are coarsely quantised. Their 1-min medians (Section 2.3) take values in steps of 0.125 and 0.05 m s^{-1}, and 66–83% and 81–89% of them are multiples of 0.25 and 0.1 m s^{-1}, respectively. We therefore take 0.25 and 0.1 m s^{-1} as the resolution of the archived 5-s values of V and W.

A multiwavelength polarisation lidar (YLJ3, GBQ L-03D; Hefei Zhongke Guangbo Quantum Technology Co., Ltd., Hefei, China) stands about 10 m from the radar. It emits pulses of 98.7, 45.5 and 97.2 mJ at 355, 532 and 1064 nm at 10 Hz into a 300-mm telescope; its blind zone is 60 m, and full overlap is reached at about 0.5 km. Each profile accumulates 1200 pulses over 120 s from its time stamp, and profiles are recorded every 10 min, with the system idle in between. The instrument software provides the aerosol backscatter coefficient at the three wavelengths and the volume linear depolarisation ratio at 355 and 532 nm in 7.5-m gates (Section 2.4). A GRIMM EDM 180 optical particle counter (GRIMM Aerosol Technik, Ainring, Germany) [40] (hereafter, the counter) reported PM_{10} and 31 cumulative number channels from 0.25 to >32 μm every minute, with PM_{10} reported up to 6500 μg m^{-3}. Visibility from a forward-scatter sensor at 2 m [26], 10-m wind speed, 2-m air temperature and precipitation came from the 1-min station records. Dust samples collected at 47, 63 and 80 m on the 80-m meteorological tower at the station were sized by laser diffraction (Section 2.6). Hourly ERA5 fields [41] supplied boundary-layer height, friction velocity u_*, cloud fraction and hydrometeor mixing ratios.

All times are Beijing time (BJT, UTC+8). Local solar time is 2.42 h behind BJT (Equation (S1)). Sunrise and sunset were computed for each date; sunset was at 20:41 BJT on 26 March and at 21:19 BJT on 3 May. All heights are given above the station.

Table 1. Instruments and data.

Instrument	Specification	Analysis Use
W-band radar	Vertically pointing pulsed Doppler radar (Chengdu Yuanwang Technology Co., Ltd.), 94 GHz (wavelength 3.2 mm; 3.206 mm in the data header). Pulse combination: unmodulated 1-µs pulse from 0.15 km (150-m resolution), linear-frequency-modulated 2-µs pulse compressed to 15 m from 0.405 km. Data header: peak power 40.8 dBm, antenna gain 53 dB, beamwidths 0.3° × 0.4°, losses 6.2 dB, waveform bandwidth 10 MHz; manufacturer's configuration: antenna gain 57.9 dB, beamwidths 0.14° × 0.13°. Z, V, W and SNR every 5 s in 15-m gates	1-min medians, 0.15–4.995 km; detection at SNR ≥ -10 dB
Polarisation lidar (YLJ3, Hefei Zhongke Guangbo)	Aerosol backscatter coefficient (km^{-1} sr^{-1}; Fernald retrieval, lidar ratios 40, 50 and 40 sr) at 355, 532 and 1064 nm and volume linear depolarisation ratio at 355 and 532 nm; SNR ≥ 3; 7.5-m gates; 120-s integration every 10 min; full overlap at about 0.5 km	Window centres; detection from β_{532} at 0.30–0.99 km; δ_{532}
Particle counter	GRIMM EDM 180 [40]; PM_{10}, $PM_{2.5}$, PM_1 and 31 cumulative number channels from 0.25 to >32 µm every minute; PM_{10} reporting ceiling 6500 $\mu g m^{-3}$	Window medians; size distribution for the closure
Surface station	Forward-scatter visibility sensor at 2 m [26], 10-m wind speed, 2-m air temperature, precipitation; 1 min	Visibility groups, clear windows, class A/B
Tower samplers	Dust samples from 47, 63 and 80 m on the 80-m tower (sampler type and period not documented); laser diffraction (Mastersizer 2000, Malvern Instruments Ltd., Malvern, UK), 53 bins, 0.42–631 µm	Size distributions including giant particles
ERA5	Hourly, 0.25°; boundary-layer height, u_* (single levels); cloud fraction and cloud liquid, cloud ice, rain and snow mixing ratios (pressure levels) [41]	Hydrometeor screening of elevated echoes; case context

2.2. Data Matching and Classification

To match the instruments in time, we centred a 10-min window on each lidar profile, spanning $[t-5, t+5)$ min. A window is complete when the surface station, the counter and the radar each provide at least seven valid minutes; 2082 of the 2160 possible windows (96.4%) are complete. Valid radar minutes without any detection count as echo-free. Figure 2 summarises the processing chain. The windows are grouped by median surface visibility into five groups (Table 2), and we refer to windows with visibility below 0.5 km as heavy dust. Clear windows have PM_{10} below 150 $\mu g m^{-3}$, visibility of at least 10 km and no precipitation (714 windows).

Biological echoes depend on temperature and on time after sunset (Section 3.3). To separate them from dust echoes, we also divided the windows into two classes of biological-echo risk. Class A (low risk) comprises windows outside the first 4 h after sunset with 2-m air temperature below 10 °C, together with night-time windows (from 4 h after sunset to sunrise) below 15 °C. Class B (high risk) comprises all other windows. The two classes differ sharply in clear air: mean echo occurrence at 0.15–0.48 km was 0.008 in clear class-A windows ($n = 245$) and 0.56 in clear class-B windows ($n = 469$). None of the 26 clear daytime windows colder than 10 °C, all in the early morning, contained echo, consistent with the temperature dependence of insect flight [36]. The first 4 h after sunset are excluded from class A because clear windows colder than 10 °C still had a mean occurrence of 0.33 at 2–4 h after sunset (25 windows on 4 days). The separation does not depend on the exact thresholds: temperature thresholds of 8–12 °C and exclusion periods of 3–5 h give clear-air

occurrences of 0.002–0.025 in class A and 0.53–0.60 in class B (Text S2; Table S1). Of the 2082 windows, 624 are class A and 1458 are class B.

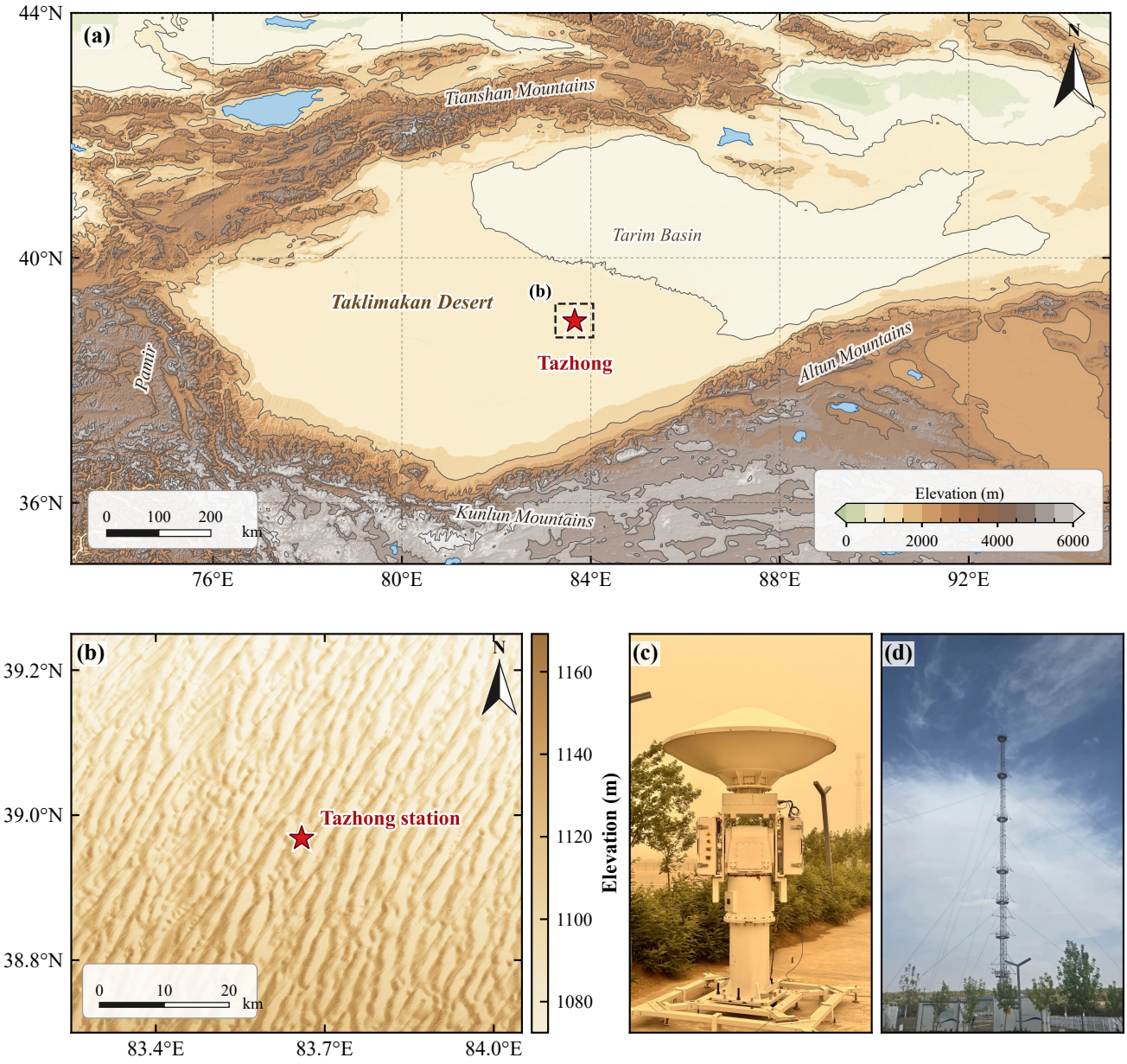


Figure 1. Study area. (**a**) Topography of the Tarim Basin (ETOPO 2022 [42]); the star marks Tazhong station. (**b**) Dune topography around the station (Copernicus GLO-30 [43]). (**c**) The W-band radar at Tazhong. (**d**) The 80-m meteorological tower and planted vegetation at Tazhong station (summer view).

All class-A windows with visibility below 0.5 km fall on 26 March, 04:18–20:38 BJT (99 windows); we refer to this period as the cold storm. The comparisons in Sections 3.3 and 3.4 use the 30-m cells of the joint detection grid (Section 2.5), grouped into five sets. Class-A dust cells are radar-detected cells with valid lidar backscatter in class-A windows with visibility below 1 km; all of them fall in the cold storm. Warm-season dust cells are radar-detected cells with valid lidar backscatter in class-B windows with 2-m temperature of at least 15 °C and visibility below 3 km, excluding 26 March. Clear-air echo cells are radar-detected cells in clear class-B windows; for the lidar comparison, they are restricted to windows with echo occurrence of at least 0.5 at 0.15–0.48 km and to cells with valid lidar

backscatter. Clear-air no-echo cells are cells with valid lidar backscatter in clear windows without echo at 0.15–0.48 km, and moderate-dust cells are cells with valid lidar backscatter in windows with visibility of 1–10 km.

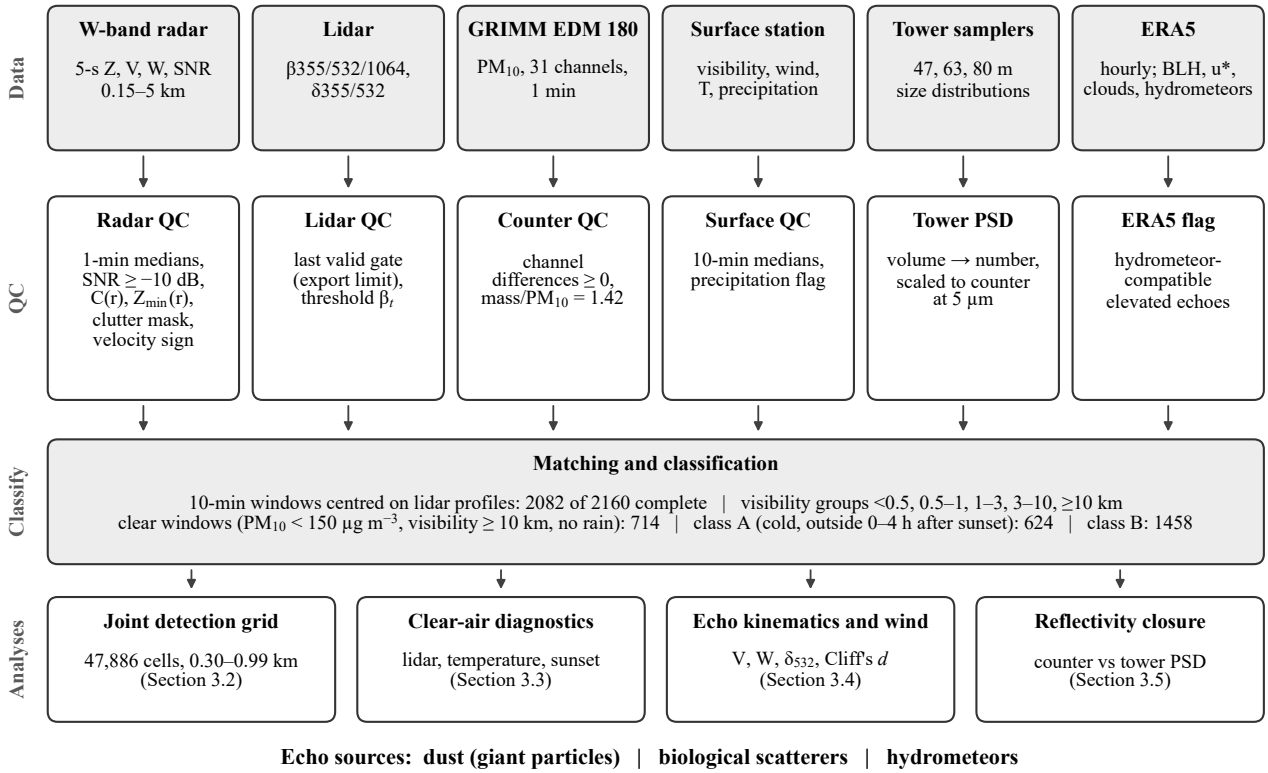


Figure 2. Data flow from the six data sources through quality control, matching and classification to the four analyses of Sections 3.2–3.5. The bottom row lists the three echo sources considered.

Table 2. Complete 10-min windows by surface visibility and class (number of days in parentheses), and the number of the seven surface-defined dust events with windows in each group. The windows come from five continuous observation blocks. Clear windows have $PM_{10} < 150$ µg m^{-3}, visibility ≥ 10 km and no precipitation.

Visibility (km)	All	Class A	Class B	Events
<0.5	222 (3)	99 (1)	123 (3)	3
0.5–1	22 (3)	0	22 (3)	3
1–3	299 (8)	57 (2)	242 (8)	6
3–10	808 (12)	222 (7)	586 (12)	6
≥10	731 (10)	246 (7)	485 (10)	1
All	2082 (15)	624 (13)	1458 (15)	7
Clear	714 (10)	245 (7)	469 (10)	–

2.3. Radar Processing, Sensitivity and Calibration

We reduced the radar moments to 1-min medians and retained a minute when at least 10 of its 12 records were valid. A gate counts as detected when SNR ≥ -10 dB. To describe how often echo is present, we define the echo occurrence of a height band b in a window as

$$O_b = \frac{1}{M} \sum_{m=1}^{M} \mathbb{I}\Big(\sum_{g \in b} E_{m,g} > 0 \Big), \tag{1}$$

where M is the number of valid minutes, $E_{m,g} = 1$ when gate g is detected in minute m, and $\mathbb{I}$ equals 1 when its argument holds. O_b is thus the fraction of minutes with echo

anywhere in the band. We use four bands: 0.15–0.48 km (near-surface), 0.48–1.0 km (low), 1–3 km and 3–5 km. A daily mask for fixed returns (detection frequency ≥ 0.80, median $|V| \leq 0.15\ \mathrm{m\,s^{-1}}$ and median $W \leq 0.25\ \mathrm{m\,s^{-1}}$) changed no occurrence value. The main conclusions also hold for stricter detection thresholds. Raising the threshold to -8 or -6 dB lowers the radar-only fraction in heavy dust (Section 3.2) from 4.7% to 4.0% and 3.4%; clear-air occurrence stays below 0.01 in class-A windows and falls to 0.50 and 0.42 in class-B windows (Table S2b).

The radar's sensitivity can be derived from the archived data themselves. For each gate at range r, we define the processing constant

$$C(r) = Z - \mathrm{SNR} - 20\log_{10}\left(\frac{r}{r_0}\right) \tag{2}$$

as the median over all detections at that gate, with Z in dBZ, SNR in dB, and $r_0 = 1$ km. The minimum detectable reflectivity then follows as

$$Z_{\min}(r) = C(r) + \mathrm{SNR}_t + 20\log_{10}\left(\frac{r}{r_0}\right), \tag{3}$$

with the detection threshold $\mathrm{SNR}_t = -10$ dB (Figure 3a). $Z_{\min}$ rises from -38.1 dBZ at 0.21 km to -32.7 dBZ at 0.39 km. Above the splice, it is -34.4, -32.9, -29.7 and -26.6 dBZ at 0.405, 0.48, 0.70 and 1.0 km. These values agree with an empirical estimate, the median archived Z at SNR between -10.5 and -9.5 dB, at the middle of each band (Table S2a).

To check whether the archived reflectivity is consistent with the radar hardware, we compared the processing constant with values computed from the radar equation (Equation (S2); [44]). The constant reflects the pulse combination (Figure 3a). At 0.21–0.39 km, it is -14.5 dBZ, which agrees with the value computed for the unmodulated 1-µs pulse from the parameters in the data header (peak power 40.8 dBm, antenna gain 53 dB, beamwidths $0.3^\circ \times 0.4^\circ$, losses 6.2 dB, receiver bandwidth 10 MHz): -14.6 dBZ for a noise figure of 5.4 dB and -17.0 to -13.0 dBZ for noise figures of 3–7 dB. Above the splice, the constant is -16.6 dBZ, within the range of -20.0 to -16.0 dBZ computed for the 2-µs pulse. It shows no further step at larger ranges: the empirical $Z_{\min}$ at 1–3 and 3–5 km agrees with the value computed from this constant to within 0.5 dB (Table S2a). The gates at 0.15–0.195 km, at the edge of the blind zone of the 1-µs pulse, have constants of -9.3 to -13.6 dBZ.

Three alternative assumptions change the computed constants. The radar configuration given in the same documentation lists a higher antenna gain (57.9 dB) and narrower beams ($0.14^\circ \times 0.13^\circ$) than the data header, which lowers the computed constants by 1.7 dB (Text S3). A water reference of $|K_w|^2 = 0.93$ instead of 0.75 lowers them by 0.9 dB, whereas a reflectivity referenced to dust ($|K_d|^2 = 0.166$; Section 2.6) would raise them by 6.5 dB. The archived reflectivity therefore agrees with the radar parameters to within 3 dB. These parameters, however, were not checked against an external target such as rain [21]. We therefore also test the closure against a deliberately large 10-dB overestimate of the archived reflectivity (Section 3.5).

Two further properties of the archived data affect the analysis. First, across the splice, the reflectivity of continuous targets drops by 4.25 dB, whereas SNR drops by only 1.0 dB ($n = 798$ min). We therefore report reflectivity separately below and above 0.39–0.405 km; echo occurrence depends only on SNR and is unaffected. Second, negative velocities denote downward motion: in the precipitation echoes at 3–5 km on 3 May, 89–95% of the gate-minutes with SNR > 0 dB had negative velocities (median -0.75 to $-1.0\ \mathrm{m\,s^{-1}}$; Figure S1).

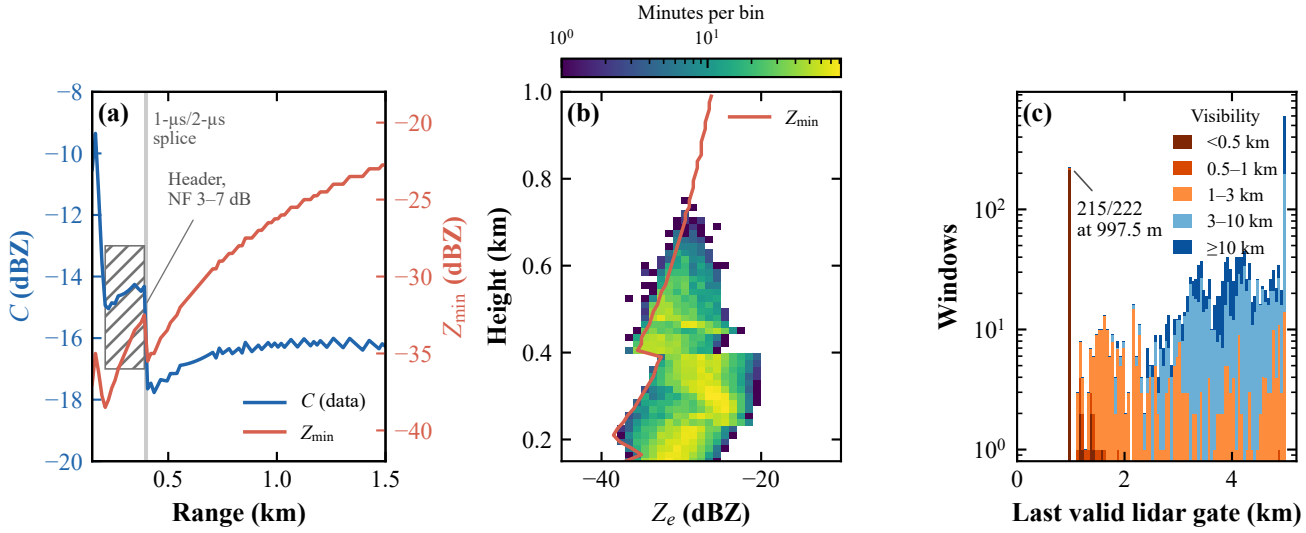


Figure 3. Radar sensitivity and lidar profile extent. (**a**) Processing constant C (blue, left axis) and minimum detectable reflectivity $Z_{\min}$ (red, right axis) versus range; the grey band marks the splice of the 1-µs and 2-µs pulses, and the hatched box shows the constant computed from the header parameters for noise figures of 3–7 dB. (**b**) Distribution of reflectivity with height on 26 March 2025, 16:00–24:00 BJT (colour: minutes per bin), with $Z_{\min}$ (red). (**c**) Height of the last valid lidar gate by visibility group; 215 of the 222 heavy-dust profiles end at 997.5 m, where the quality control of the lidar software (SNR $\geq$ 3) truncates them.

2.4. Lidar Data and Detection Criterion

The backscatter coefficients are retrieved by the instrument software with the Fernald method, using lidar ratios of 40, 50 and 40 sr at 355, 532 and 1064 nm and a reference height of 25–30 km, and the molecular contribution is removed. Because the retrieval assumes fixed lidar ratios, we use the values only for detection and relative comparisons. The gain ratio of the depolarisation channels was calibrated with the $\pm 45^{\circ}$ method on 17 March 2025 [19]. The software subtracts the background, applies an overlap correction and removes clouds and noise, and it exports only gates with a signal-to-noise ratio of at least 3; other gates are set to NaN. We used these products without independent calibration. Because full overlap is reached at about 0.5 km, the lidar values at 0.30–0.50 km depend on the overlap correction; we therefore also repeated the comparison for 0.51–0.99 km (Table S7). An important property of the archived profiles is where they end. In heavy dust, 215 of 222 profiles (96.8%) ended at exactly 997.5 m, as did 9 of 22 profiles at visibility of 0.5–1 km, whereas no profile at visibility of 1 km or more ended there (Figure 3c; Table S3; Text S4). Other profiles extend to 5 km. According to the manufacturer, the profiles end at 997.5 m because the signal above this height failed the quality-control criterion of SNR $\geq$ 3. That almost all heavy-dust profiles end at the same height shows that the criterion truncates the profile at a fixed height of about 1 km, not at the last gate with sufficient signal. In heavy dust, the lidar product therefore contains no valid data above 1 km, but the profile end does not mark the height at which the signal was lost. Within 0.30–0.9975 km, we evaluate lidar detection from the backscatter values. A 30-m cell is lidar-detected when at least three of its four gates hold finite positive β_{532}, and the cell median is at least $\beta_t = 1 \times 10^{-4}$ km^{-1} sr^{-1}. This threshold is about one-twentieth of the median clear-air β_{532} at 0.3–1 km (2.0–2.2 $\times 10^{-3}$ km^{-1} sr^{-1}); thresholds of 3×10^{-5} and 3×10^{-4} are used to test the sensitivity.

2.5. Joint Detection Grid

To compare the two instruments on a common basis, we divided 0.30–0.99 km in each window into 23 cells of 30 m. Each cell contains two radar gates and four lidar gates, and the 2082 windows give 47,886 cells. The grid starts at 0.30 km, one 150-m pulse length above the edge of the radar's blind zone, so that the lowest radar gates, whose processing constants are anomalous at 0.15–0.195 km (Section 2.3), do not enter. Starting the grid at this height does not inflate the radar-only fraction: at 0.21–0.30 km, both instruments detected 95% of the heavy-dust cells, and the radar alone detected none, so including these heights would lower the radar-only fraction. A cell is radar-detected ($R = 1$) when at least 20% of the valid minutes contain a detection in either gate and lidar-detected ($L = 1$) by the criterion of Section 2.4. Because the two criteria sample time differently (minute occurrence within the 10-min window versus a single 2-min profile), the category fractions describe these criteria rather than absolute detection limits. Every cell in the complete windows had a lidar profile within 2 min and at least seven valid radar minutes, so all cells could be evaluated; the 78 incomplete windows are excluded. Below the pulse splice at 0.405 km, the 1-µs pulse has a range resolution of 150 m, five times the cell height, so radar detections in the four lowest cells (0.30–0.42 km) can include echo from neighbouring heights; above the splice, the radar resolution (15 m) is finer than the cells. To test whether this mismatch affects the results, we repeated the comparison for 0.42–0.99 km only and with both instruments aggregated to 150-m cells (Table S7). The lidar integrates over the 2 min that follow the window centre, so we also repeated the comparison with the radar detection evaluated only in these 2 min (Table S7). Each cell falls into one of four categories:

$$\text{category} = \begin{cases} \text{both}, & R = 1,\ L = 1, \\ \text{radar only}, & R = 1,\ L = 0, \\ \text{lidar only}, & R = 0,\ L = 1, \\ \text{neither}, & R = 0,\ L = 0. \end{cases} \tag{4}$$

2.6. Size Distributions and Reflectivity Closure

To identify which particle sizes produce the radar echo, we computed reflectivity from two sets of size distributions, one from the counter and one from the tower samples, and compared it with the observation.

The counter reports cumulative concentrations $N(> d_i)$ in L^{-1} at 31 thresholds d_i, from which we derive bin concentrations and diameters:

$$\begin{aligned} \Delta N_i &= \max[N(> d_i) - N(> d_{i+1}),\, 0], \\ D_i &= \sqrt{d_i d_{i+1}}. \end{aligned} \tag{5}$$

The duplicated 2.5-µm channel gives $\Delta N = 0$. As an internal plausibility check, we computed mass from the bins with a particle density of 2.65 g cm^{-3} (Equation (S3)). It was 1.42 times PM_{10} (10th–90th percentiles 1.15–2.05), or 1.41 times without the 81 windows in which PM_{10} reached its reporting ceiling, and no adjacent channel difference was negative (Figure S2; Text S5). This check shows that the channels are internally consistent; it does not validate the concentrations. PM_{10} is defined by a 50% cut at 10 µm aerodynamic diameter, which corresponds to about 6–7 µm volume-equivalent diameter for mineral dust with a density of 2.65 g cm^{-3} and dynamic shape factors of 1.0–1.4 [45]. The counter sizes particles by an optical equivalent diameter and the tower analysis by laser diffraction; we do not correct for the difference between these diameters.

The counter's open channel above 32 µm (median 4.0 L^{-1} in the closure period) has no upper size bound and is therefore not part of the computed size distribution. Assigning

it to diameters of 32–40 µm would raise the computed reflectivity by 4.1 dB in the median window and by up to 5.0 dB in single windows. Instead of assigning a size, we use the channel as a constraint: we compute the equivalent diameter at which these particles would supply the difference between observed and computed reflectivity (Section 3.5).

The tower samples were sized by laser diffraction (Mastersizer 2000) in 53 bins between 0.42 and 631 µm. The sampler type and sampling period are not documented, and the samples were not collected during the radar observations analysed here. Two effects make the scaled tower distributions upper estimates of the giant-particle tail at radar height. First, passive samplers collect large grains more efficiently than fine ones. Second, the samples come from 47–80 m, below the radar heights. To combine the shape of the tower distributions with the absolute concentration measured by the counter, we converted the volume percentages v_i to relative number concentrations and scaled them to the counter's concentration above $D_s = 5$ µm during the closure period:

$$n_i = \frac{v_i}{D_i^3}, \qquad N_i = n_i \frac{N_G(> D_s)}{\sum_{j:\, D_j > D_s} n_j}, \tag{6}$$

where N_G is the counter's cumulative concentration; a bin that straddles D_s is split log-uniformly. Scaling at 2.5 and 10 µm tests the sensitivity to D_s; this range is shown as shading and error bars in Section 3.5.

For particles much smaller than the wavelength, the equivalent reflectivity factor is

$$\begin{aligned} Z_e &= \frac{|K_d|^2}{|K_w|^2}\, 10^{-15} \sum_i N_i D_i^6, \\ |K|^2 &= \left| \frac{\varepsilon - 1}{\varepsilon + 2} \right|^2, \end{aligned} \tag{7}$$

with Z_e in mm^6 m^{-3}, N_i in L^{-1} and D_i in µm. We use the usual W-band value $|K_w|^2 = 0.75$ and $|K_d|^2 = 0.166$, which follows from the permittivity of Tazhong dust at 94 GHz, $\varepsilon_d = 3.06 - 0.17i$, derived for a moisture content of 0.9% [26]. To account for uncertainty in these factors, we vary the ratio $|K_d|^2/|K_w|^2 = 0.22$ from 0.18 to 0.34. This range includes a water reference of 0.93 (ratio 0.18) and dry-mineral permittivities up to about 4.1, and it changes Z_e by -0.9 to $+1.9$ dB. The Rayleigh approximation remains adequate for the largest grains: for the corresponding refractive index $m = 1.75 - 0.05i$, Mie backscatter at 94 GHz differs from the Rayleigh value by -0.03 dB at 150 µm and by less than 0.6 dB up to 631 µm. We therefore apply Equation (7), with this small Mie correction, to the full size distributions.

To identify which sizes dominate the echo, we use the cumulative reflectivity of particles up to diameter D,

$$Z_e(\leq D) = \frac{|K_d|^2}{|K_w|^2}\, 10^{-15} \sum_{i:\, D_i \leq D} N_i D_i^6, \tag{8}$$

and find the diameter at which it reaches a given value by linear interpolation in $\log D$ between bin edges. We report three quantities: Δ, the median over the windows of observed minus computed reflectivity; D_{obs}, the diameter at which the cumulative reflectivity reaches the observed median; and $D_{\mathrm{obs}-10}$, the diameter at which it reaches the observed median minus 10 dB. Particles smaller than $D_{\mathrm{obs}-10}$ therefore produce less than one-tenth of the observed echo.

We take the observed reflectivity from the cold storm between 16:00 BJT and sunset (16:00–20:41 BJT, 28 class-A windows). In this period, no echo occurred between 1 and 3 km,

so precipitation falling from above did not contribute to the low-level echo. The whole period 16:00–24:00 BJT (48 windows) serves as a sensitivity test. Because of the pulse splice, reflectivity is evaluated separately at 0.15–0.39 and 0.405–0.48 km. In each window, we estimate the median over all valid minutes by treating undetected minutes as weaker than $Z_{\min}$. Excluding the four lowest gates (that is, using 0.21–0.39 km) gives a median of −28.1 dBZ, 0.9 dB above the 0.15–0.39-km value; we use the latter.

To quantify how $D_{\mathrm{obs}-10}$ depends on these assumptions, we repeated the calculation in each window for all combinations of sampler height, scaling diameter (2.5, 5 and 10 μm), permittivity ratio (0.18, 0.22 and 0.34), particle shape (spheres and spheroids) and reflectivity offsets of 0, −3 and −10 dB and report the share of the observed echo produced by particles ≤32 and ≤50 μm. Because the tower samples may over-represent the giant-particle tail at radar height, we also used closure-adjusted tails, in which the tower concentrations above 32 μm are reduced, uniformly or in proportion to $(D/32\ \mu\mathrm{m})^{-\alpha}$, until the computed reflectivity equals the observation (Table S8).

2.7. ERA5 Screening and Statistics

To screen elevated echoes for cloud and precipitation, we flag an elevated echo as hydrometeor-compatible when, in the same band and hour, the ERA5 cloud fraction is at least 0.20 or the sum of the cloud liquid, cloud ice, rain and snow mixing ratios is at least 10^{-6} kg kg^{-1}. Such echoes are excluded from the dust analysis.

We compare groups of cells with Cliff's d,

$$d = \frac{1}{n_x n_y} \sum_{i=1}^{n_x} \sum_{j=1}^{n_y} \mathrm{sgn}(x_i - y_j) = P(X > Y) - P(X < Y), \tag{9}$$

which is the probability that a value from the first group exceeds one from the second, minus the reverse probability. It is 0 when values from either group are equally likely to be the larger and $|d| = 1$ when the two distributions do not overlap. With several thousand cells per group, p-values do not discriminate between groups and are not reported. Because neighbouring windows are autocorrelated, all intervals come from block resampling. The 95% interval of d comes from 2000 replicates that resample the days of each group with replacement, or 60-min blocks of windows for a group that comes from a single day. Intervals for cell fractions come from 2000 replicates that resample 60-min blocks of windows. The association between a counter-based size index and echo occurrence (Text S6; Table S4) was evaluated with a hierarchical block bootstrap over observation blocks and dust events (5000 replicates, 60-min circular blocks; [46]).

3. Results

3.1. Three Cases, Three Kinds of Echo

Figure 4 presents three cases that illustrate the three kinds of echo recorded during the campaign: dust in the cold storm of 26 March, echo of uncertain source in warm-season dust on 11 April and hydrometeors on 3 May. Sections 3.2–3.5 then test these attributions with all 2082 windows.

The cold storm of 26 March was cold, windy and very dense. Between 16:00 and 24:00 BJT, the 2-m air temperature was 4.7–6.6 °C, and PM_{10} had a median of 4370 μg m^{-3} and reached the 6500-μg m^{-3} reporting ceiling in 40% of the windows. Visibility had a median of 227 m, and the 10-m wind speed had a median of 9.1 m s^{-1} (Figure 4(a1)). The lidar backscatter was strongest below about 0.7 km, δ_{532} was about 0.25, and every profile ended at 997.5 m (Figure 4(b1,c1)). The radar recorded a continuous echo between 0.15 and about 0.7 km, with reflectivity of −35 to −25 dBZ and weak downward velocities

(Figure 4(d1,e1)). This echo was not caused by precipitation: no precipitation was recorded at the surface, no echo occurred between 1 and 3 km, and the hydrometeor-compatible echo at 3–5 km near 16:00 BJT was not connected to the low-level echo. The windows after sunset (20:41 BJT) belong to class B by definition (red strip in Figure 4), although the storm continued. The echo, however, did not change at sunset: the median reflectivity at 0.15–0.39 km was −29.1 dBZ before and −28.9 dBZ after it.

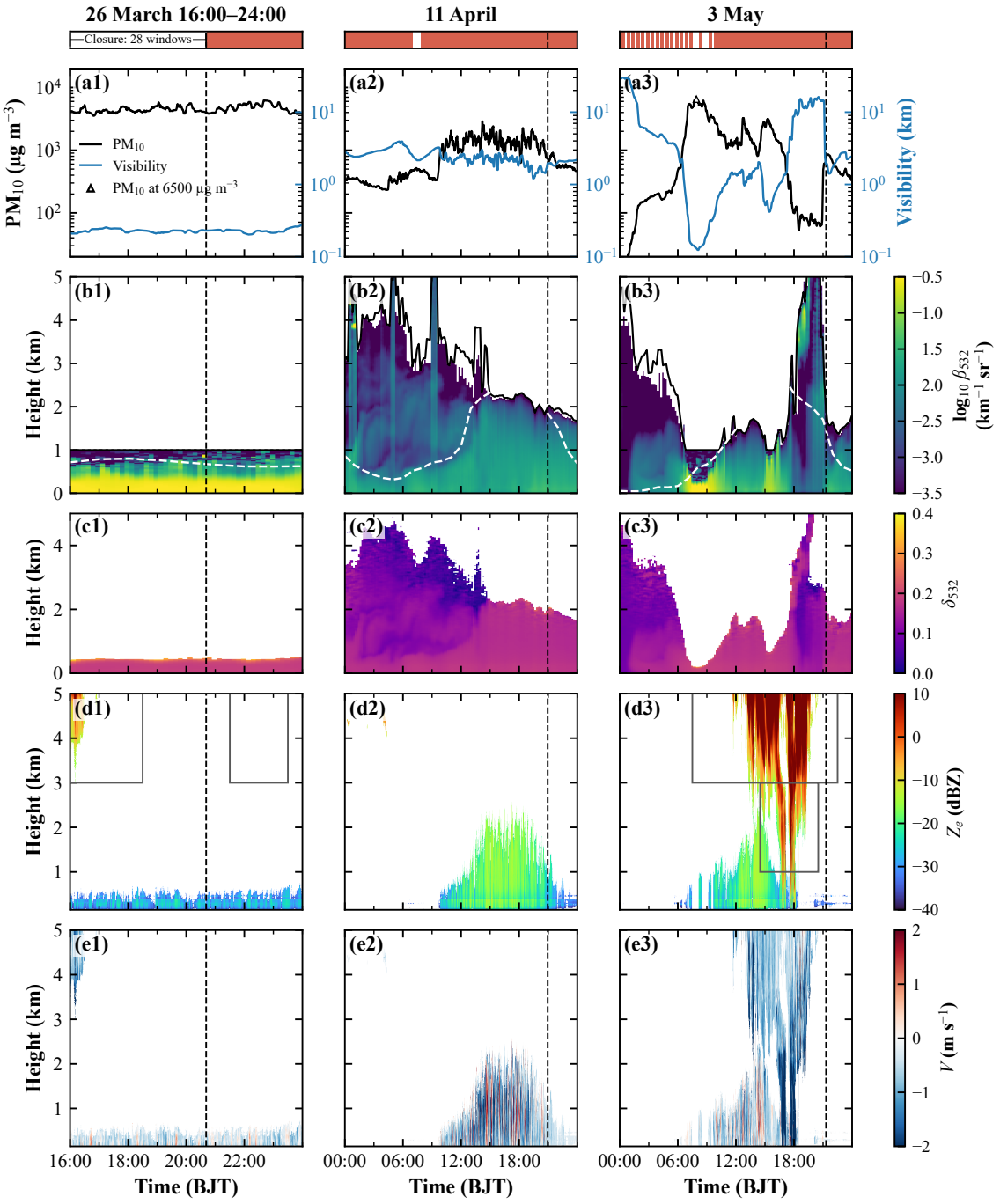


Figure 4. Three cases: 26 March 2025, 16:00–24:00 BJT (left), 11 April (centre) and 3 May (right). (**a1**–**a3**) PM_{10} (black) and visibility (blue); triangle: 10-min median PM_{10} at the 6500-μg m^{-3} ceiling. (**b1**–**b3**) 532-nm backscatter, with the last valid lidar gate (black) and the ERA5 boundary-layer height (white dashed). (**c1**–**c3**) 532-nm depolarisation ratio. (**d1**–**d3**) Reflectivity; grey boxes mark hydrometeor-compatible ERA5 environments. (**e1**–**e3**) Doppler velocity (negative downward). Top strips: class A (white) and class B (red); dashed lines: sunset. The bracket in the top strip of the left

column marks the 28 class-A windows (16:00–20:41 BJT) used for the reflectivity closure (Section 3.5). The radar-only fraction of the cold storm (9.1%, Section 3.2) refers to all 99 class-A heavy-dust windows of 26 March (04:18–20:38 BJT), not only to the period shown.

The case of 11 April shows warm-season dust with an echo of uncertain source. After 10:00 BJT, hourly median PM_{10} rose from 400–500 to 1000–1900 $\mu g\,m^{-3}$, visibility fell to 1–3 km, and the lidar showed a dust layer 2–4 km deep (Figure 4(a2–c2)); the 2-m air temperature reached 22 °C. The radar recorded echo below 0.5 km from about 06:00 BJT and echo extending above 1 km from 12:10 to 21:20 BJT. Over the day, the 90th percentile of the echo top was 2.2 km, reflectivity was −30.0 to −14.5 dBZ (5th–95th percentiles), and the velocities alternated in sign (Figure 4(d2,e2)). None of the 55 windows with echo at 1–3 km were hydrometeor-compatible in ERA5. Around sunset (20:57 BJT), the echo top descended from 1.6 km at 20:00 to 0.7 km at 21:30 BJT, at 0.13–0.17 $m\,s^{-1}$ (from a linear fit to the 5-min echo tops and from the end points), with 5-min median velocities of −0.25 to −0.75 $m\,s^{-1}$ at 1–2 km. This slow descent argues against settling giant grains, because particles large enough to produce −30 to −15 dBZ without a lidar signature would settle at 0.6 $m\,s^{-1}$ or faster. Meanwhile, the lidar backscatter and depolarisation at 1–2.5 km did not decrease (median β_{532} of 3.7×10^{-3} and 5.3×10^{-3} $km^{-1}\,sr^{-1}$, and δ_{532} of 0.166 and 0.160, in the 2 h before and after 21:20 BJT), and below 1 km, the echo persisted until midnight at 16–19 °C. Nevertheless, the case alone cannot decide whether this echo came from dust or from biological scatterers (Section 3.4).

On 3 May, dust was followed by hydrometeor echoes aloft. At about 08:20 BJT, the 10-min median PM_{10} peaked at 5300 $\mu g\,m^{-3}$, visibility fell to 137 m, and the lidar profiles shortened to about 1 km (Figure 4(a3,b3)). Between 11:33 and 20:43 BJT, the radar recorded echoes at 3–5 km of −12.5 to +21.5 dBZ (5th–95th percentiles), with median velocities of −0.75 to −1.0 $m\,s^{-1}$ in 0.5-km bands (Figure 4(d3,e3)). All 55 windows with these echoes were hydrometeor-compatible in ERA5. Over the whole campaign, hydrometeors were also common aloft: 89.6% of the windows with echo at 3–5 km (537 of 599) and 36.7% of those with echo at 1–3 km (201 of 547) were hydrometeor-compatible (Table S5). The remaining analysis therefore concentrates on the lowest kilometre.

3.2. The Radar Echo Lies Mostly Within the Layer of Valid Lidar Backscatter

In heavy dust, the radar alone detected few cells (Figure 5; Table 3). These fractions compare the archived products at the detection thresholds of Sections 2.4 and 2.5, and their values depend on these thresholds. At visibility below 0.5 km (222 windows on 3 days, 5106 cells), 37.7% of the cells between 0.30 and 0.99 km were detected by both instruments, 4.7% by the radar only (95% interval 1.9–7.9%), 43.8% by the lidar only and 13.7% by neither. Varying the lidar threshold from 3×10^{-5} to 3×10^{-4} changed the radar-only fraction to 1.2–5.8%. In the cold storm (all 99 class-A heavy-dust windows, 04:18–20:38 BJT on 26 March; 2277 cells), the radar-only fraction was higher, at 9.1% (3.5–15.2%; 2.3–11.0% across thresholds). All of these radar-only cells occurred in the densest phase of the storm, at a median visibility of 168 m, while hydrometeor echoes were present above 1.5 km. Their Doppler velocity and spectral width (−0.25 and 0.45 $m\,s^{-1}$) matched those of the cells detected by both instruments (−0.25 and 0.40 $m\,s^{-1}$). A contribution from falling hydrometeors, however, cannot be excluded, so not all of these cells need contain dust. At all other visibilities, the radar-only fraction was at most 1.0%. Seen from the lidar side, the lidar backscatter fell below the threshold in 18% of the heavy-dust cells, and the radar detected echo in one quarter of these cells (25%; 13–35%), or in 32% (17–44%) in the cold storm. These fractions depend little on the coarse resolution of the lowest cells: for 0.42–0.99 km only, the radar-only fraction was 4.9% (2.2–8.3%) in heavy dust and 9.5% in the cold storm, and with both instruments aggregated to 150-m cells, it was 5.6% and 11.6%

(Table S7). With the radar evaluated only during the 2-min lidar integration, the radar-only fraction fell to 3.6% in heavy dust and 6.9% in the cold storm, so the 10-min radar criterion slightly favoured the radar; for 0.51–0.99 km, above full overlap, it was 4.6% and 8.6%. Even if all lidar detections above 0.5 km were invalid, the radar-only fraction in heavy dust would be 17.1% (Table S7).

The height profiles of the cold-storm cells explain why the radar added so few cells (Figure 5e). The radar detected 100% of the cells at 0.30–0.42 km but only 46% at 0.60 km, 22% at 0.72 km and 6% at 0.96 km. The lidar detected 78% at 0.60 km, 52% at 0.75 km and 25% at 0.96 km, and above 0.5 km, it detected at least as many cells as the radar at every height. Radar-only cells made up 10–15% of the cells at 0.36–0.75 km. The radar detection rate fell with height for two reasons: the dust echo weakened with height, and Z_{min} rose by 6.3 dB between 0.48 and 1.0 km (Figure 3a,b). Above about 0.7 km, the radar therefore detected few cells irrespective of the lidar data.

Because lidar-only cells form the largest category in heavy dust, we checked whether these lidar values are internally consistent (Text S4; representative profiles in Figure S3). Four checks support most of them. All exported backscatter values passed the manufacturer's quality-control criterion of SNR $\geq$ 3 (Section 2.4). In the lidar-only cells, backscatter was valid at all three wavelengths; 98% of the lidar-detected cells were also detected at the same height in an adjacent window; and the median δ_{532} (0.17, interquartile range 0.16–0.18) exceeded the clear-air value (0.11). This δ_{532} value is not a fill value of the product: it decreased from 0.18 at 0.33 km to 0.15–0.16 above 0.7 km and took about 100 distinct values, and the six heavy-dust cells with valid δ_{532} that neither instrument detected had 0.11. The median β_{532} decreased smoothly by more than three orders of magnitude between 0.30 and 0.96 km. Because the backscatter is retrieved with a fixed lidar ratio, and below 0.5 km depends on the overlap correction, the size of this decrease is uncertain; we use the values only for detection and relative comparisons. Individual profiles in the densest dust were less regular (Figure S3): in 10 windows, all at visibility below 150 m, β_{532} dropped abruptly at 0.29–0.39 km while β_{355} and β_{1064} did not, and above about 0.5 km, the values fluctuated strongly between adjacent gates, as expected near the noise level. The abrupt drop can turn cells into radar-only cells: these 10 windows contained 27.6% of the radar-only cells, and without them, the radar-only fraction was 3.5%. The fluctuations can add spurious lidar detections: treating cells in which β_{532} varied by more than a factor of 10 as not detected by the lidar (10.6% of the lidar-detected cells) raised the radar-only fraction to 6.7% or to 6.1–7.2% for factors of 30 and 5 (Table S7).

The lidar data also constrain the vertical structure of the storm. A surface visibility of 168 m corresponds to an extinction coefficient of about 23 km^{-1}, which would extinguish the lidar signal well below 0.3 km if it extended upward. If the backscatter at 0.3–0.9 km is signal rather than noise, extinction must have decreased steeply above the surface; the retrieved values do not allow this decrease to be quantified. Above 1 km, the heavy-dust profiles contain no valid lidar data (Section 2.4; Figure 3c), so any radar echo there lies beyond the lidar product. At 1.0–1.5 km, outside hydrometeor-compatible environments, the radar detected echo in 1.7% of the heavy-dust cells and in none of the cold-storm cells (Table S11). Including windows in hydrometeor-compatible environments raised these values to 9.0% and 12.3%, with a median Doppler velocity of -2.1 m s^{-1}, consistent with falling hydrometeors. The radar therefore added little vertical coverage to the lidar, both below and above 1 km; its contribution lies instead in what its echo measures (Section 3.5).

In clear air, the picture is different. At visibility of 10 km or more, 22.2% of the cells were detected by both instruments: 33.5% in class B but only 0.1% in class A. In these cells, the radar echo coincided with the background aerosol signal of the lidar; Section 3.3 identifies its source.

Table 3. Joint radar–lidar detection at 0.30–0.99 km by surface visibility and class: percentages of 30-m cells in each category (Equation (4)) for the lidar threshold $\beta_t = 1 \times 10^{-4}$ km^{-1} sr^{-1}. The range given for radar only spans $\beta_t = 3 \times 10^{-5}$ to 3×10^{-4}.

Visibility (km)	Class	Windows	Cells	Both (%)	Radar Only (%)	Lidar Only (%)	Neither (%)
<0.5	All	222	5106	37.7	4.7 (1.2–5.8)	43.8	13.7
	A	99	2277	40.5	9.1 (2.3–11.0)	31.2	19.2
	B	123	2829	35.5	1.1 (0.2–1.7)	54.0	9.4
0.5–1	All	22	506	72.7	1.0 (0.2–1.4)	26.1	0.2
	A	0	0	–	–	–	–
	B	22	506	72.7	1.0 (0.2–1.4)	26.1	0.2
1–3	All	299	6877	48.1	0.0 (0.0–0.2)	51.6	0.2
	A	57	1311	3.1	0.0	96.9	0.0
	B	242	5566	58.7	0.0 (0.0–0.3)	41.0	0.3
3–10	All	808	18584	21.1	0.6 (0.2–0.7)	78.0	0.4
	A	222	5106	0.0	0.0	100.0	0.0
	B	586	13478	29.1	0.8 (0.3–0.9)	69.6	0.6
≥10	All	731	16813	22.2	0.0 (0.0–0.3)	77.4	0.4
	A	246	5658	0.1	0.0	99.9	0.0
	B	485	11155	33.5	0.0 (0.0–0.4)	66.0	0.6
All	All	2082	47886	27.7	0.7 (0.2–1.0)	69.8	1.8
	A	624	14352	6.8	1.4 (0.4–1.7)	88.8	3.0
	B	1458	33534	36.6	0.4 (0.1–0.7)	61.7	1.3

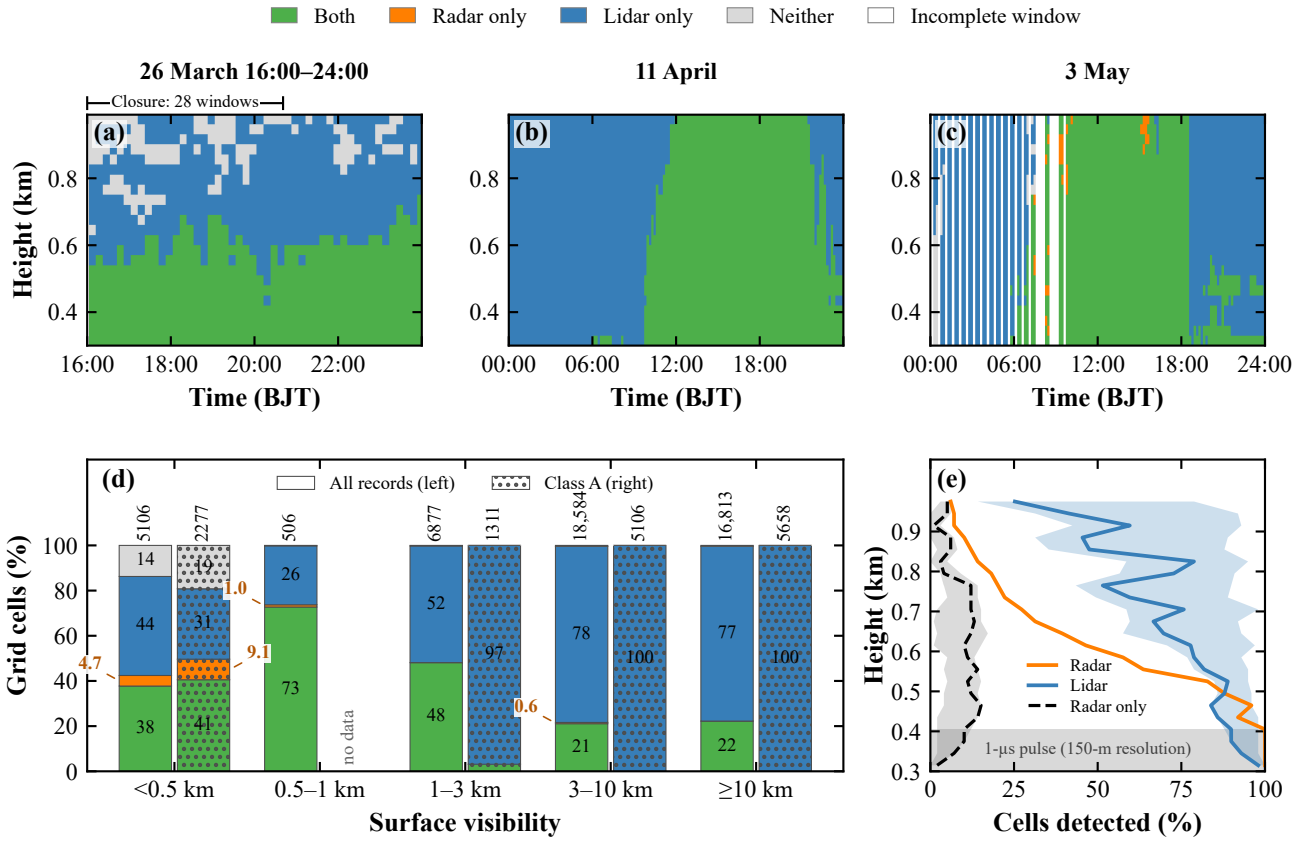


Figure 5. Joint radar–lidar detection at 0.30–0.99 km. (**a**–**c**) Detection category of each cell for the three cases (white: incomplete windows). (**d**) Category fractions by visibility for all windows (left bar of each pair) and class A (right bar); numbers are cell counts. The class-A bar at visibility below 0.5 km comprises all 99 class-A heavy-dust windows of 26 March (04:18–20:38 BJT), whereas (**a**) shows only

16:00–24:00 BJT; the bracket above (**a**) marks the 28 windows used for the reflectivity closure. (**e**) Detection rates of the radar and the lidar, and the radar-only fraction, versus height in the cold storm (all 99 windows); the grey band marks 0.30–0.405 km, where the 1-µs pulse has a range resolution of 150 m; shading spans lidar thresholds of 3×10^{-5} to 3×10^{-4} km^{-1} sr^{-1}.

3.3. Biological Echoes in Clear Warm Air

In clear warm air, frequent low-level echoes were most likely produced by biological scatterers (Figure 6). This attribution is indirect: no biological sampling was made, so it rests on the behaviour of the echoes and on the exclusion of other sources. We reached it in three steps: we characterised the echoes, tested whether sparse giant grains could produce them and excluded Bragg scattering from refractive-index fluctuations. Table S9 lists all candidate sources that we considered, with the signature each would produce and the observations that test it.

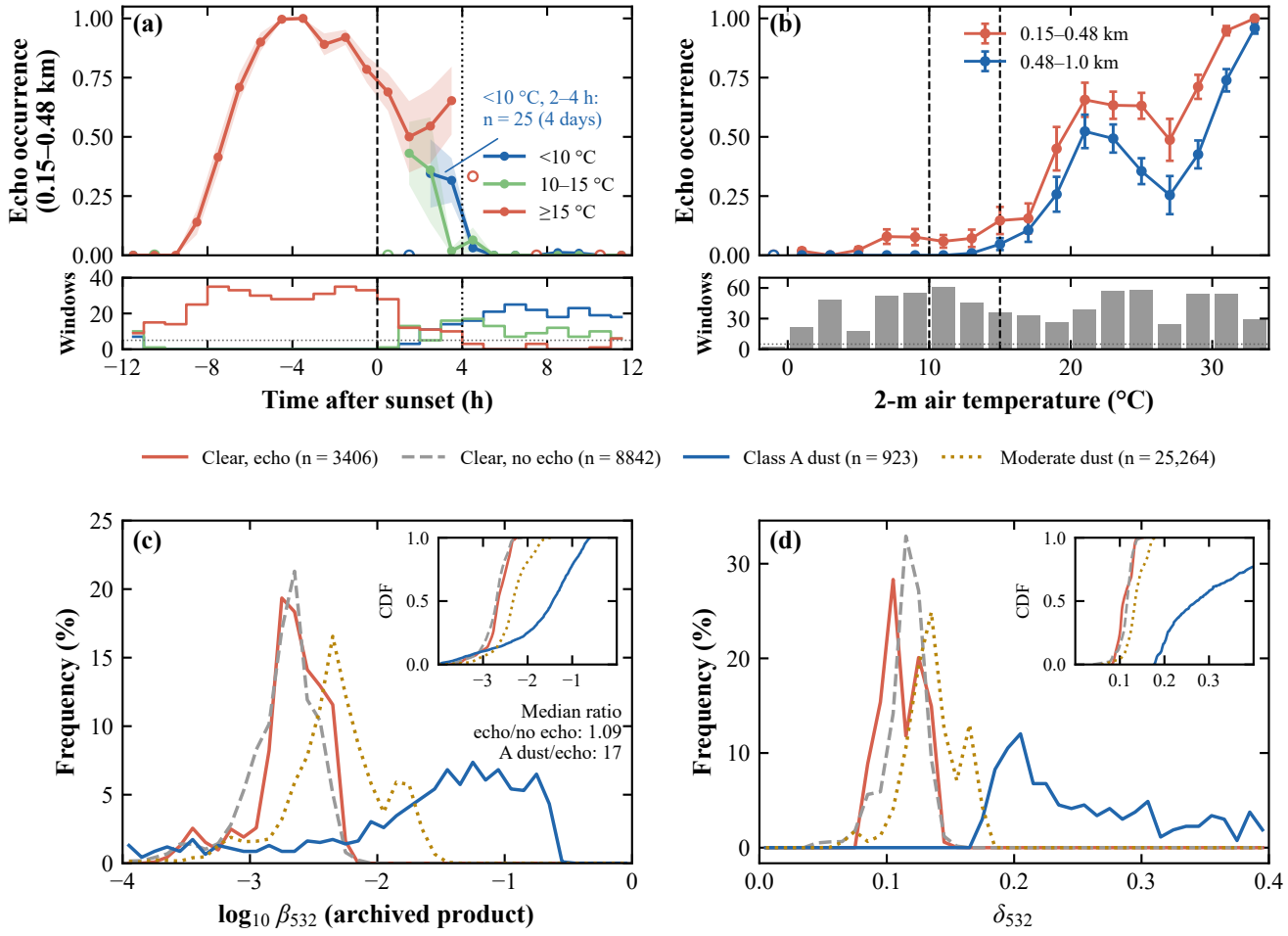


Figure 6. Biological echoes in clear air. (**a**) Echo occurrence at 0.15–0.48 km versus time after sunset for three temperature ranges, in 1-h bins; lines show the mean over windows and shading ±1 standard error of the mean. The lower strip gives the number of windows per bin; open symbols mark bins with fewer than 5 windows, for which no shading is drawn. (**b**) Echo occurrence at 0.15–0.48 and 0.48–1.0 km versus 2-m air temperature in 2- °C bins (bars: ±1 standard error); the lower strip gives the number of windows per bin, and open symbols mark bins with fewer than 5 windows. Sample counts are listed in Table S10. (**c**) 532-nm backscatter and (**d**) depolarisation ratio for clear-air cells with and without echo, class-A dust cells and moderate-dust cells; insets show cumulative distributions.

The echoes were frequent, strongly temperature dependent and invisible to the lidar. Echo occurrence at 0.15–0.48 km was 0.91 on clear afternoons (local solar time 12:00–18:00,

temperature ≥ 15 °C). It was at most 0.08 below 14 °C, 0.45 at 18–20 °C, 0.66 at 20–22 °C and 0.95–1.00 above 30 °C (Figure 6b). Over all clear class-B windows, low-level echo was present in 56% of the minutes. Median β_{532} in clear cells with radar echo, however, exceeded that in clear cells without echo by only 9% (ratio 1.09), and δ_{532} was 0.108 and 0.117, respectively. Class-A dust cells, in contrast, had 17 times higher β_{532} and a δ_{532} of 0.27 (Figure 6c,d). Echo occurrence was also nearly independent from wind: mean occurrence was 0.89–1.00 in all wind classes from 0 to more than 6 m s^{-1} (Figure 7d).

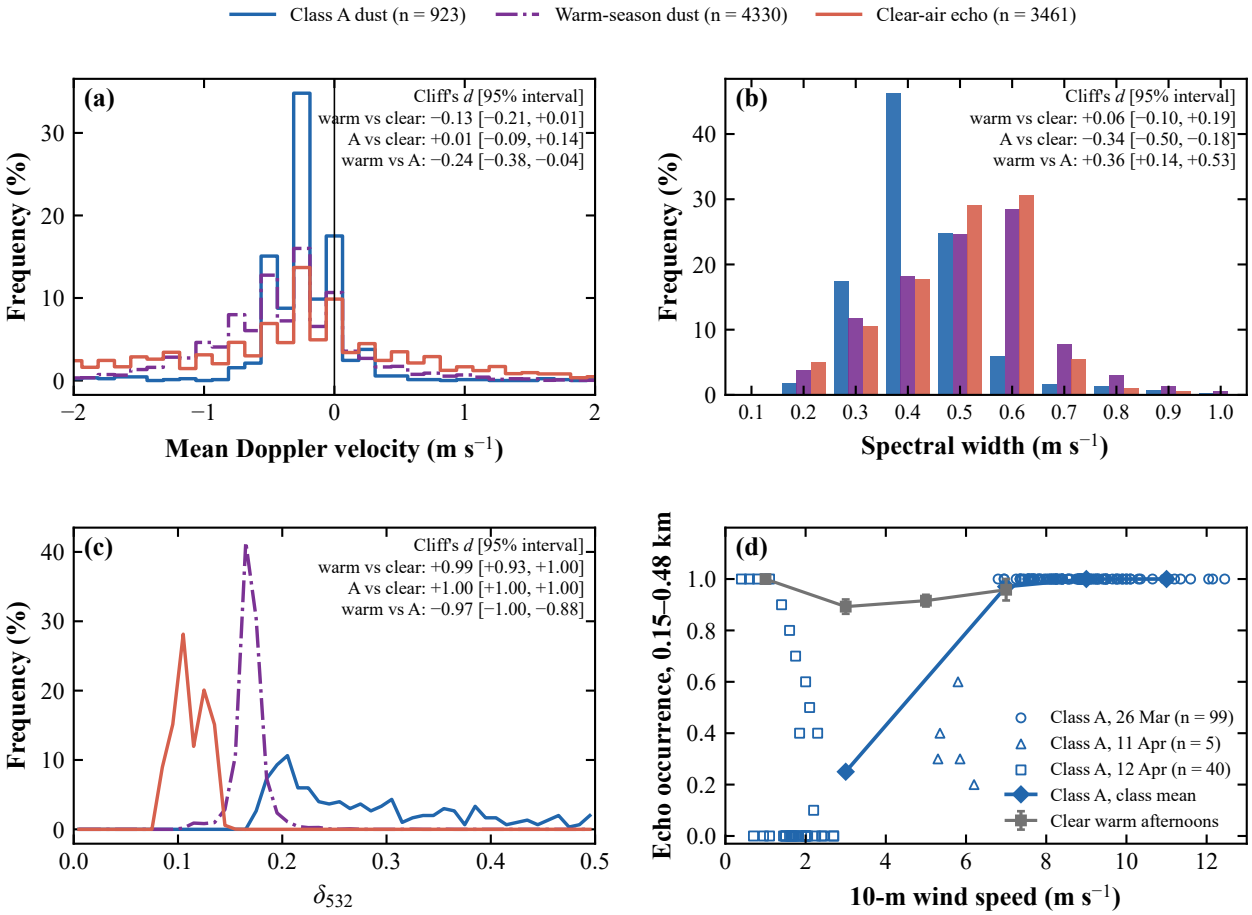


Figure 7. Radar and lidar properties of dust and biological echoes. (**a**) Doppler velocity, (**b**) spectral width and (**c**) 532-nm depolarisation ratio for class-A dust, warm-season dust and clear-air echo cells; each panel gives Cliff's *d* and its 95% interval for each pair of groups. (**d**) Echo occurrence at 0.15–0.48 km versus 10-m wind speed for class-A windows with $PM_{10} \geq 400$ µg m^{-3} (symbols by date) and for clear warm afternoons (grey).

Sparse giant grains are the main alternative explanation, because they could raise radar reflectivity without a lidar signature. An echo of −30 dBZ requires about 0.4 grains L^{-1} of 150 µm or 70 grains m^{-3} of 200 µm; the extinction of these grains (0.014 and 0.005 km^{-1}) would be detected by neither the lidar nor the visibility sensor. Such grains, however, fall at 1–1.5 m s^{-1} and remain aloft only with convective or wind-driven support. The clear-air echoes behaved differently: they persisted after sunset, when daytime convection had decayed. At temperatures of at least 15 °C, occurrence was 0.63 in the first 2 h and 0.60 at 2–4 h after sunset, and it fell to zero more than 5 h after sunset (10 windows; 0.002 over all 220 clear windows; Figure 6a). In these evening windows, the wind was weak (median 0.9 m s^{-1}), and the echoes had a median Doppler velocity of −0.25 m s^{-1} (interquartile range −0.25 to −0.06 m s^{-1}; the median equals the lower quartile because of the quantisation, Section 2.1). This is a fraction of the fall speed of such grains; in still air,

grains falling at 1 m s^{-1} would leave the 0.15–0.48-km layer within 6 min. The echoes also occurred at wind speeds below 2 m s^{-1}. Two forms of lofting could supply such grains, and neither fit the observations. Wind-driven saltation requires winds above the threshold for sand motion, whereas echo occurrence did not depend on wind speed (Figure 7d). Dust devils are intermittent and local, so a vertically pointing beam would sample them only occasionally; they would also raise the lidar backscatter through the fine dust they carry, and they are largely confined to the daytime [47].

Bragg scattering from refractive-index fluctuations, the other common source of clear-air echoes at centimetre wavelengths [48], is negligible at 3.2 mm. From $\eta = 0.38\, C_n^2 \lambda^{-1/3}$ [49], its equivalent reflectivity is below −59 dBZ even for a large refractive-index structure parameter of $C_n^2 = 10^{-12}$ m$^{-2/3}$, more than 20 dB below $Z_{\min}$. With giant grains, Bragg scattering and the other candidates in Table S9 excluded, biological scatterers, most likely insects, are the explanation most consistent with the observations. This attribution agrees with cloud-radar studies, in which insects dominate the clear-air returns in the boundary layer and their flight depends on temperature [34–36]; similar clear-air echoes are recorded by millimetre-wave cloud radars in China [38]. The planted trees and the vegetated shelterbelt beside the station (Figure 1d), an unusual habitat within the dune field, are a plausible source of these scatterers. Separating windows of low and high biological-echo risk is therefore a precondition for every radar statistic of dust that follows.

3.4. Separating Dust Echoes from Biological Echoes

If the radar moments differed between dust and biological echoes, they could be used to separate the two in warm dusty weather. They did not (Figure 7a–c). Warm-season dust cells (4330 cells on 7 days) and clear-air echo cells (3461 cells on 8 days) had nearly identical distributions of spectral width (Cliff's $d = 0.06$; 95% interval −0.10 to 0.19). Their medians and interquartile ranges were identical, 0.50 (0.40–0.60) m s^{-1}, which partly reflects the 0.1-m s^{-1} resolution of the archived widths (Section 2.1). Their velocities also differed little (medians −0.44 and −0.25 m s^{-1}; $d = -0.13$). Class-A dust cells, all from the cold storm, had narrower widths (median 0.40, interquartile range 0.40–0.50 m s^{-1}; $d = -0.34$ against clear-air echoes, interval −0.50 to −0.18). The two distributions overlap substantially, and the difference may reflect the different turbulence of a cold, windy storm as much as the different target.

The lidar, by contrast, separated the three groups clearly. The depolarisation ratio in the same cells was 0.27 for cold-storm dust, 0.17 for warm-season dust and 0.11 for clear-air echoes ($|d| \geq 0.97$ between each pair; the interval of [1.00, 1.00] arises because the distributions do not overlap). The lidar thus confirms that dust was present in the warm-season dust cells, but single-frequency Doppler moments cannot tell whether the radar echoes there came from dust or from biological scatterers. We therefore exclude these cells from the size analysis.

Within class A, where biological echoes are rare, dust echo occurrence varied strongly between days. Occurrence at 0.15–0.48 km was close to 1 only on 26 March, when both wind (median 8.8 m s^{-1}; ERA5 friction velocity 0.69 m s^{-1}) and PM_{10} (5200 μg m^{-3}) were high (Figure 7d; Table S6). On 12 April, with a median wind of 1.75 m s^{-1} and PM_{10} of 470 μg m^{-3}, occurrence ranged from 0 to 1 (mean 0.24 over 40 windows), and on 11 April, it was 0.36 (5 windows). Because wind and loading rose together, and no class-A window on another day had wind of at least 6 m s^{-1}, these data cannot separate their effects. Both effects are physically plausible: strong wind lifts and suspends giant grains, and high loading supplies more of them.

3.5. Reflectivity Closure: Particles Larger than About 50 μm Produce the Echo

In the cold storm, the observed reflectivity required particles larger than 32 μm, and under nominal calibration, mainly particles larger than about 50 μm (Figure 8; Table 4). Between 16:00 BJT and sunset (28 windows), the observed reflectivity was −29.1 dBZ at 0.15–0.39 km (interquartile range −30.1 to −27.5 dBZ) and −32.2 dBZ at 0.405–0.48 km. At 0.405–0.48 km, where the radar resolution is 15 m, the counter fell short of the observation by 23.8 dB, and $D_{\mathrm{obs}-10}$ of the tower distributions was 51–58 μm (Table 4), slightly smaller than at 0.15–0.39 km because the observed reflectivity there is 3 dB lower; the size result therefore does not depend on the 150-m resolution of the lowest band. Three observations show that this was a dust echo rather than a biological one: it occurred at 5.4–6.6 °C, where clear-air echo occurrence was at most 0.08 (Figure 6b); the co-located δ_{532} of the cold-storm cells was 0.27; and the reflectivity did not change across sunset.

The two sets of size distributions bracket the observation. Reflectivity computed from the counter's closed channels (0.25–32 μm) was −56.0 dBZ, 27.1 dB below the observation in the median window (21.6–29.7 dB over the 28 windows; Figure 8a). The full tower distributions, which over-represent the largest grains (Section 2.6), exceeded the observation by 10.2, 6.5 and 3.4 dB for the samples from 47, 63 and 80 m in the median window (1.1–13.3 dB across scalings).

The tower distributions also show which sizes produce the echo. Up to 32 μm, they gave only −50.6 to −51.9 dBZ, more than 20 dB below the observation, whereas up to 150 μm, they gave −25.9, −29.4 and −28.3 dBZ. Their cumulative reflectivity reached the observed median at 113–157 μm (91–222 μm across scalings; Figure 8b). Under nominal calibration, particles smaller than 44–85 μm produced less than one-tenth of the observed reflectivity across all scalings, permittivities and particle shapes, so particles larger than about 50 μm produced at least 81% (at least 90% for the nominal permittivity) of the echo, and particles larger than 32 μm at least 97% (Table S8). Between 49% and 61% of the sample volume was in particles larger than 52 μm (Figure 8c2). The counter's own open channel leads to the same conclusion: its 4.0 L^{-1} above 32 μm would supply the missing reflectivity if their equivalent diameter were 108 μm (81–135 μm in single windows). The result also holds for the longer period. For the whole period 16:00–24:00 BJT, including the 20 class-B windows after sunset, the counter deficit was 26.3 dB, the tower excess was 3.4–10.2 dB in the median window as in the main period (3.6–10.4 dB for the period-mean size distribution), and the closure diameter was 111–154 μm.

Two kinds of uncertainty affect this result: parameter uncertainties, which can be computed, and representativeness uncertainties, which cannot. For the counter, we combined three parameter uncertainties in the direction that reduces the deficit. The permittivity range raises the computed reflectivity by at most 1.9 dB, assigning the open channel to 32–40 μm raises it by up to 5.0 dB in single windows, and a 10-dB overestimate of the archived reflectivity would lower the observation by 10 dB. Even with all three applied together, the counter still fell short of the observation by 4.9 dB in the closest window and by 11.7 dB in the median window. Non-spherical shapes, which Equation (7) ignores, would raise all computed values by a further 0.1–1.1 dB for spheroids with aspect ratios up to 2 (Rayleigh approximation; [50]), leaving a deficit of 3.8 dB in the closest window. The particles in the counter's closed channels ($\leq$32 μm) therefore cannot produce the observed echo.

Two effects that cannot be quantified here would only strengthen this conclusion. First, the counter samples at the surface, and because dust concentration usually decreases with height above a source, it overstates the concentration at 0.15–0.39 km. Second, sand deposited on the radar antenna or its cover during the storm would lower the archived reflectivity. Both effects make the counter deficit a lower bound and the tower excess an upper bound.

For the tower distributions, the scaling diameter changes the computed reflectivity by −2.7 to +3.0 dB, the permittivity by −0.9 to +1.9 dB and non-sphericity by up to +1.1 dB. Together, these are comparable to the smallest tower excess (3.4 dB at 80 m). A 10-dB overestimate of the archived reflectivity would shift the diameter required for closure from 113–157 µm to 60–70 µm and $D_{\mathrm{obs}-10}$ to 24–47 µm; a 3-dB overestimate would shift $D_{\mathrm{obs}-10}$ to 37–70 µm (Table S8). The 50-µm statement therefore holds under nominal calibration. For a 3-dB overestimate, particles ≤50 µm would produce 5–9% of the echo for the nominal parameters but up to 36% in the least favourable combination, and for a 10-dB overestimate, the statement does not hold; particles smaller than 32 µm would still produce at most 5.5% of the echo for a 3-dB and 27.7% for a 10-dB overestimate. The two parts of the result depend differently on the tower samples. The deficit of the counter's closed channels and the open-channel constraint do not depend on them. Producing the observed reflectivity with 50-µm grains alone would require 359 L^{-1}, or 62 mg m^{-3}, 9.8 times the mass computed from the counter at the surface (Table S8). The value of $D_{\mathrm{obs}-10}$, in contrast, depends on the shape of the tower distributions above 32 µm. A tail that is over-represented in the tower samples, as their excess over the observation suggests, does not change the conclusion: with closure-adjusted tails, $D_{\mathrm{obs}-10}$ was 53–114 µm, and particles ≤50 µm produced at most 8.8% of the echo. Two aspects lie beyond what the available samples can constrain: how the size distribution changed between the sampling times and the radar observation, and how efficiently the samplers collected each size (Section 2.6).

The counter and the tower samples also diverge in a size-dependent way. Compared with the tower distributions scaled at 5 µm, the counter recorded 0.5–0.6 of the particles larger than 10 µm, 0.2–0.3 of those larger than 20 µm and 0.05–0.10 of those larger than 32 µm. This decrease with size is expected from size-dependent inlet losses of the counter and size-dependent collection by the samplers, but the two causes cannot be separated here. In summary, the W-band echo in this storm was a measure of particles larger than 32 µm, mainly larger than about 50 µm, which PM_{10} and lidar backscatter do not constrain and the counter does not size.

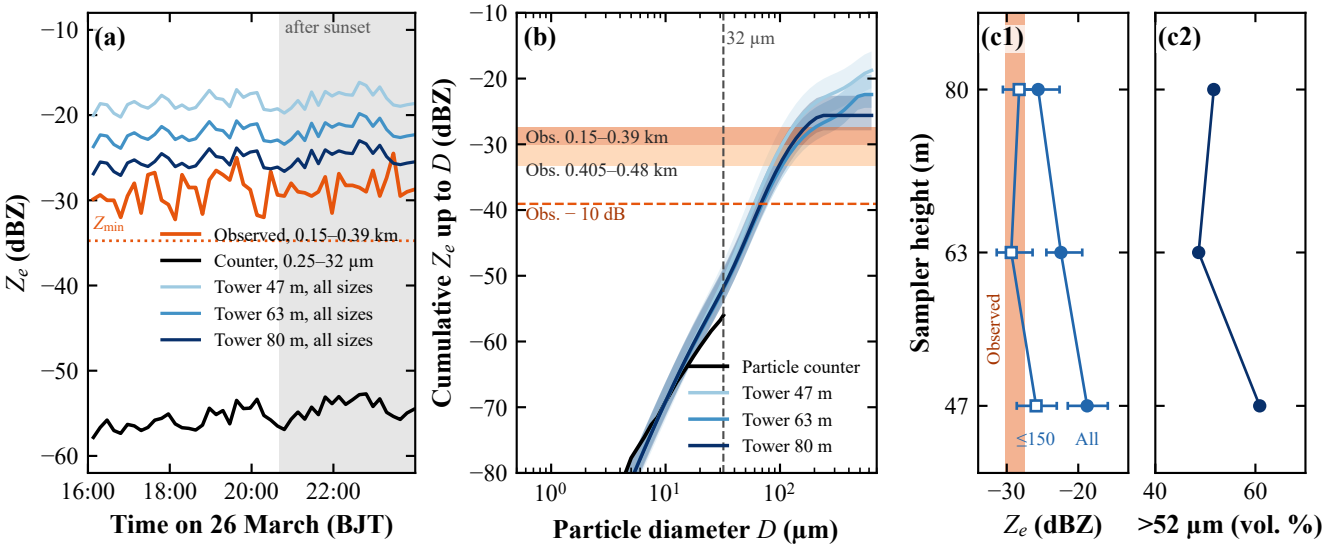


Figure 8. Reflectivity closure in the cold storm of 26 March 2025. (**a**) Observed reflectivity and reflectivity computed from the counter and tower size distributions in each window, 16:00–24:00 BJT (grey: windows after sunset). (**b**) Cumulative reflectivity up to diameter D for 16:00–20:41 BJT, with the observed range (bands) and the observation minus 10 dB (dashed); where a curve crosses the dashed line gives $D_{\mathrm{obs}-10}$. (**c1**) Computed reflectivity for all sizes (filled) and for $D \leq 150$ µm (open) versus sampler height. (**c2**) Volume fraction above 52 µm.

Table 4. Reflectivity closure for the cold storm on 26 March 2025, 16:00–20:41 BJT (28 class-A windows). Tower distributions are scaled to the counter at 5 µm (scaling at 2.5–10 µm in parentheses). Observed Z_e: −29.1 dBZ at 0.15–0.39 km (interquartile range −30.1 to −27.5 dBZ) and −32.2 dBZ at 0.405–0.48 km (−33.3 to −30.2 dBZ); Z_{min} is −34.8 and −34.2 dBZ. Upper part: 0.15–0.39 km; lower part: 0.405–0.48 km, where the radar resolution is 15 m (computed Z_e as in the upper part).

Size Distribution	Computed Z_e (dBZ)				Δ (dB)	D_{obs} (µm)	D_{obs-10} (µm)
	≤32 µm	≤100 µm	≤150 µm	All Sizes			
0.15–0.39 km (1-µs pulse, 150-m resolution; observed −29.1 dBZ)							
Particle counter (0.25–32 µm)	−56.0	–	–	–	+27.1	–	–
Open channel: 4.0 L^{-1} above 32 µm would supply the remainder at an equivalent diameter of 108 µm (81–135 µm in single windows)							
Tower 47 m (0.42–631 µm)	−50.6	−30.5	−25.9	−18.8 (−21.5 to −15.9)	−10.2	113 (91–144)	60 (52–70)
Tower 63 m (0.42–631 µm)	−51.9	−33.7	−29.4	−22.4 (−24.5 to −19.4)	−6.5	157 (115–222)	70 (59–80)
Tower 80 m (0.42–631 µm)	−51.7	−32.9	−28.3	−25.6 (−27.9 to −22.6)	−3.4	139 (107–181)	68 (57–78)
0.405–0.48 km (2-µs pulse, 15-m resolution; observed −32.2 dBZ)							
Particle counter (0.25–32 µm)			as above		+23.8	–	–
Tower 47 m (0.42–631 µm)			as above		−13.2	90 (75–109)	51 (44–59)
Tower 63 m (0.42–631 µm)			as above		−9.6	114 (90–138)	58 (49–66)
Tower 80 m (0.42–631 µm)			as above		−6.4	106 (86–128)	57 (48–65)

4. Discussion

4.1. Radar–Lidar Complementarity in Dense Dust

Combined radar–lidar observations of dust have been motivated by the expectation that the radar observes dust beyond the height at which the lidar signal is extinguished [28,30,31], as it does for cloud droplets [51]. Within the lowest kilometre at Tazhong, this expectation was met only in part. Between 0.30 and 0.99 km, the radar alone detected 4.7% of the heavy-dust cells, which is one quarter of the cells in which the archived lidar backscatter fell below the threshold. In the cold storm, the radar-only fraction was 9.1%, all during the densest phase. Above 0.5 km, the radar detected no more cells than the lidar at any height, because the dust echo weakened with height while the radar's sensitivity decreased with range.

The lidar profiles in heavy dust ended at 997.5 m, where the quality control of the lidar software truncated them. A profile end set by such a criterion is not an extinction height: it shows only that the signal above a fixed height did not reach the threshold. Before the top of an archived lidar profile is interpreted as the height at which the lidar lost the dust, the quality-control rules of the product should therefore be checked. Above this end, outside hydrometeor-compatible environments, the radar detected echo in only 1.7% of the heavy-dust cells at 1.0–1.5 km (Section 3.2).

4.2. What W-Band Dust Echoes Measure

Reflectivity–mass (Z–M) relations at Tazhong relate wind-profiler, Ka-band or W-band reflectivity to PM_{10} [23,24,26]. The two quantities, however, are dominated by very different particles. PM_{10} is defined by a 50% cut at 10 µm aerodynamic diameter, about 6–7 µm volume-equivalent diameter for mineral dust, whereas in the cold storm, particles larger than 32 µm produced more than 94% of the echo, and particles larger than about 50 µm produced most of it. A Z–M relation calibrated with PM_{10} therefore holds only while the giant-particle fraction changes in step with PM_{10}. This fraction depends on the wind and turbulence that keep giant grains aloft, so it can differ between events. Across all windows, the partial rank correlation between the counter-based size index and low-level echo occurrence was 0.35 (bootstrap 95% interval 0.20–0.41), after adjusting for PM_{10} and wind speed, and 0.20 (−0.06 to 0.37), after also adjusting for temperature and local time (Table S4). This modest association agrees with the closure result that the counter does not

size the particles that dominate the echo. Its decrease after the second adjustment indicates that part of the unadjusted association reflects biological activity.

The same sensitivity is also an opportunity. Giant particles are underrepresented in models and in routine measurements [5–8], and their lofting near sources is poorly observed [9]. In the cold, windy storm, the W-band radar recorded their presence continuously in the lowest few hundred metres, under conditions of low biological-echo risk (class A). The three instruments therefore complement each other in particle size rather than in height: the lidar and the counter describe fine and coarse dust, and the radar adds the giant particles. Resolving the size of these particles will require information beyond reflectivity, such as Doppler spectra.

4.3. Biological Echoes as the Main Confounder in Warm Seasons

Insect echoes are a known contaminant of cloud-radar records at mid-latitude sites [34,35,37] and must be separated from aerosol echoes in cloud-radar studies of giant aerosol [29]. Their effect on radar records of dense dust near a major source, however, had not been quantified. At Tazhong, echoes that were most likely biological were present in 91% of the minutes of clear warm afternoons, in the same layer as the dust echoes. Their persistence after sunset in calm air and their slow descent argue against sparse giant grains as their source. Dividing the records into classes of low and high biological-echo risk reduces the risk of biological contamination, but at a cost: it also removes the warm daytime dust records. Only 624 of the 2082 windows remained in class A, and class-A heavy dust occurred on a single day. A more selective separation is not possible with the present data. Single-frequency Doppler moments did not distinguish warm-season dust echoes from biological echoes (spectral width $d = 0.06$), and the narrower widths of the cold-storm echoes ($d = -0.34$) may reflect turbulence as much as target type. Attributing warm-season dust echoes therefore requires Doppler spectra or polarimetric information [37]. We do not infer that the echoes recorded in warm-season dust were biological: the Doppler moments could not tell, and the lidar showed that dust was present ($\delta_{532} = 0.17$). Our conclusion for warm-season dust is therefore limited to the statement that its radar echo cannot be attributed to dust without additional information. Direct verification would require insect sampling at several heights, for example, with light or suction traps, together with Doppler spectra or polarimetric radar measurements during warm dust events.

The vegetated shelterbelt beside the Tazhong station probably raises the frequency of biological echoes above that over open dunes. Staffed desert stations, however, are commonly sited at roads, oases or settlements with vegetation, and the deep afternoon boundary layer of the Taklimakan [1,2] can carry insects through the lowest kilometres. Similar contamination may therefore occur at other desert sites with vegetation nearby.

4.4. Limitations

Five limitations bound these results. First, the closure rests on one storm and on tower samples collected at another time, at 47–80 m and with samplers of unknown collection efficiency. It brackets the observation and shows which sizes can produce the echo, but it does not give the size distribution at radar height. Closure-adjusted tails bound the effect of an over-represented giant tail on $D_{\mathrm{obs}-10}$ (Table S8), but the temporal representativeness of the samples remains unknown. Second, the radar parameters were not checked against an external target, and the data header and the manufacturer's configuration differ in antenna gain and beamwidth by the equivalent of 1.7 dB. A 10-dB overestimate of the archived reflectivity would shift the diameter required for closure from 113–157 μm to 60–70 μm and $D_{\mathrm{obs}-10}$ to 24–47 μm and would leave the counter deficit at 4.9 dB or more. Third, the lidar data are retrievals with fixed lidar ratios, and the exported products do

not include the raw signals, so their quality was assessed through the software's SNR criterion and the profile checks and sensitivity tests of Section 3.2; archiving the raw signals in future campaigns will allow an independent assessment. In heavy dust, the profiles end at 997.5 m, where the quality control truncates them, so above 1 km, the radar could be compared only with the absence of lidar data. Fourth, the cold heavy-dust records come from a single storm, and wind and particle loading co-varied across the three cold dust days. Fifth, the biological attribution rests on the thermal and kinematic behaviour of the echoes and on the exclusion of other sources (Table S9); no insects were sampled directly, so the attribution remains indirect.

5. Conclusions

We used collocated W-band radar, lidar, particle-counter and tower observations on 15 spring days at Tazhong to test whether a W-band radar detects dust that a lidar misses, which low-level echoes come from dust, and which particle sizes produce the dust echo. The observations lead to three conclusions.

1. In heavy dust below 1 km, the radar seldom detected dust that the lidar product missed. Radar-only cells made up 4.7% (95% interval 1.9–7.9%) of the cells between 0.30 and 0.99 km and 9.1% in the cold storm of 26 March. These fractions compare the archived products at fixed detection thresholds. The lidar profiles ended at 1 km, where the product's quality control truncated them, and above this end, outside hydrometeor-compatible environments, the radar detected echo in only 1.7% of the cells up to 1.5 km.
2. In clear warm air, frequent low-level echoes without a lidar signature were most likely produced by biological scatterers; the attribution is indirect, because no biological sampling was made. They followed temperature and time after sunset, persisted for hours after sunset in calm air and moved downward at a median of about 0.25 m s^{-1}, far more slowly than giant grains fall. Mean Doppler velocity and spectral width did not separate them from echoes in warm-season dust.
3. In the cold, windy storm, the counter's 0.25–32-µm particles produced 27 dB less reflectivity than observed, whereas the tower size distributions produced 3.4–10.2 dB more. Particles larger than 32 µm produced more than 94% of the echo for calibration errors up to 3 dB, and particles larger than about 50 µm at least 81% (at least 90% for the nominal permittivity) under nominal calibration; for a 10-dB overestimate of the archived reflectivity, the second threshold would fall to 24–47 µm.

These results suggest three practices for radar studies of dust: check the quality-control rules of archived lidar products before interpreting the top of a profile as an extinction height; screen warm-season radar records for biological echoes, for example, by temperature and time after sunset; and treat reflectivity–PM_{10} relations as dependent on the giant-particle fraction, which PM_{10} does not measure. Doppler spectra, polarimetric measurements and raw lidar signals would allow these tests to be extended to warm-season dust and to verify the composition of the echo above the end of the lidar profiles.

Supplementary Materials: The following supporting information can be downloaded at: https://www.mdpi.com/article/10.3390/rs18234105/s1, Text S1: Time conventions and dust events; Text S2: Sensitivity of the class definition; Text S3: Radar pulses, radar equation, processing constant and velocity sign; Text S4: Last valid gate, quality control and internal consistency of the archived lidar profiles; Text S5: Particle counter: quality control and size index; Text S6: Hierarchical bootstrap of the size-index association; Table S1: Sensitivity of the class definition to its thresholds; Table S2: Radar processing constant, minimum detectable reflectivity and sensitivity of the main results to the detection threshold; Table S3: Last valid gate of the archived 532-nm lidar profiles by surface

visibility; Table S4: Association between the counter size index and echo occurrence; Table S5: Elevated radar echoes in hydrometeor-compatible ERA5 environments; Table S6: Class-A windows with $PM_{10} \geq 400\ \mu g\ m^{-3}$; Table S7: Sensitivity of the joint radar–lidar detection to vertical resolution, full overlap, temporal matching, lidar validity and treatment of irregular lidar values; Table S8: Sensitivity of the size result to the tested uncertainties; Table S9: Candidate sources of the low-level clear-air echoes; Table S10: Sample counts and values behind Figure 6; Table S11: Radar detection above the end of the lidar profiles in heavy dust; Figure S1: Sign of the Doppler velocity in precipitation echoes on 3 May 2025; Figure S2: Particle-counter quality control; Figure S3: Representative heavy-dust profiles of lidar backscatter, depolarisation ratio and radar reflectivity. References [26,44,46] are cited in the Supplementary Materials.

Author Contributions: Conceptualisation, H.S.; methodology, J.L. (Jicheng Luo), M.W., H.M. and J.Z.; validation, H.S., M.W., C.Z., J.L. (Jiajun Li) and R.C.; formal analysis, H.S.; resources, J.L. (Jicheng Luo); data curation, H.S. and J.L. (Jicheng Luo); writing—original draft preparation, H.S.; writing—review and editing, M.W.; visualisation, H.S., H.M., C.Z., J.L. (Jiajun Li), J.Z. and R.C. All authors have read and agreed to the published version of the manuscript.

Funding: This research was funded by the Central Government Guidance Funds for Local Science and Technology Development Program, grant number ZYYD2025ZY21; the Youth Innovation Team of China Meteorological Administration, grant number CMA2024QN13; and the Science and Technology Development Fund of the Chinese Academy of Meteorological Sciences, grant number 2021KJ034.

Data Availability Statement: The ERA5 reanalysis data [41] are available from the Copernicus Climate Change Service Climate Data Store (https://doi.org/10.24381/cds.bd0915c6; https://doi.org/10.24381/cds.adbb2d47). The radar, lidar, particle-counter, tower and surface data from Tazhong station are available from the corresponding author on request.

Conflicts of Interest: Author Jicheng Luo is employed by Chengdu Yuanwang Technology Co., Ltd., which manufactured and supplied the W-band radar used in this study. His contributions are listed in the Author Contributions section. Apart from these contributions, the company had no role in the design of the study, the analysis and interpretation of the data, or the conclusions, and it provided no funding for this research. The remaining authors declare that the research was conducted in the absence of any commercial or financial relationships that could be construed as a potential conflict of interest. The funders had no role in the design of the study; in the collection, analyses, or interpretation of data; in the writing of the manuscript; or in the decision to publish the results.

Abbreviations

The following abbreviations are used in this manuscript:

BJT	Beijing time (UTC+8)
ERA5	Fifth-generation ECMWF atmospheric reanalysis
PM_{10}, $PM_{2.5}$	Particulate matter below 10 and 2.5 μm aerodynamic diameter
SNR	Signal-to-noise ratio
Z_e	Equivalent reflectivity factor
Z_{min}	Minimum detectable reflectivity

References

1. Wang, M.; Xu, X.; Xu, H.; Lenschow, D.H.; Zhou, M.; Zhang, J.; Wang, Y. Features of the Deep Atmospheric Boundary Layer Over the Taklimakan Desert in the Summertime and its Influence on Regional Circulation. *J. Geophys. Res. Atmos.* **2019**, *124*, 12755–12772. https://doi.org/10.1029/2019JD030714.
2. Zhang, L.; Zhang, H.; Li, Q.; Wei, W.; Cai, X.; Song, Y.; Mamtimin, A.; Wang, M.; Yang, F.; Wang, Y.; et al. Turbulent Mechanisms for the Deep Convective Boundary Layer in the Taklimakan Desert. *Geophys. Res. Lett.* **2022**, *49*, e2022GL099447. https://doi.org/10.1029/2022GL099447.
3. Zhang, L.; Zhang, H.; Cai, X.; Song, Y.; Mamtimin, A.; He, Q. Physical Mechanisms of Deep Convective Boundary Layer Leading to Dust Emission in the Taklimakan Desert. *Geophys. Res. Lett.* **2024**, *51*, e2024GL108521. https://doi.org/10.1029/2024GL108521.

4. Yang, F.; He, Q.; Huang, J.; Mamtimin, A.; Yang, X.; Huo, W.; Zhou, C.; Liu, X.; Wei, W.; Cui, C.; et al. Desert Environment and Climate Observation Network over the Taklimakan Desert. *Bull. Am. Meteorol. Soc.* **2021**, *102*, E1172–E1191. https://doi.org/10.1175/BAMS-D-20-0236.1.
5. Adebiyi, A.; Kok, J.F.; Murray, B.J.; Ryder, C.L.; Stuut, J.B.W.; Kahn, R.A.; Knippertz, P.; Formenti, P.; Mahowald, N.M.; Pérez García-Pando, C.; et al. A review of coarse mineral dust in the Earth system. *Aeolian Res.* **2023**, *60*, 100849. https://doi.org/10.1016/j.aeolia.2022.100849.
6. Ryder, C.L.; Highwood, E.J.; Walser, A.; Seibert, P.; Philipp, A.; Weinzierl, B. Coarse and giant particles are ubiquitous in Saharan dust export regions and are radiatively significant over the Sahara. *Atmos. Chem. Phys.* **2019**, *19*, 15353–15376. https://doi.org/10.5194/acp-19-15353-2019.
7. Adebiyi, A.A.; Kok, J.F. Climate models miss most of the coarse dust in the atmosphere. *Sci. Adv.* **2020**, *6*, eaaz9507. https://doi.org/10.1126/sciadv.aaz9507.
8. Kok, J.F.; Storelvmo, T.; Karydis, V.A.; Adebiyi, A.A.; Mahowald, N.M.; Evan, A.T.; He, C.; Leung, D.M. Mineral dust aerosol impacts on global climate and climate change. *Nat. Rev. Earth Environ.* **2023**, *4*, 71–86. https://doi.org/10.1038/s43017-022-00379-5.
9. Drakaki, E.; Amiridis, V.; Tsekeri, A.; Gkikas, A.; Proestakis, E.; Mallios, S.; Solomos, S.; Spyrou, C.; Marinou, E.; Ryder, C.L.; et al. Modeling coarse and giant desert dust particles. *Atmos. Chem. Phys.* **2022**, *22*, 12727–12748. https://doi.org/10.5194/acp-22-12727-2022.
10. Ratcliffe, N.G.; Ryder, C.L.; Bellouin, N.; Woodward, S.; Jones, A.; Johnson, B.; Wieland, L.M.; Dollner, M.; Gasteiger, J.; Weinzierl, B. Long-range transport of coarse mineral dust: An evaluation of the Met Office Unified Model against aircraft observations. *Atmos. Chem. Phys.* **2024**, *24*, 12161–12181. https://doi.org/10.5194/acp-24-12161-2024.
11. Freudenthaler, V.; Esselborn, M.; Wiegner, M.; Heese, B.; Tesche, M.; Ansmann, A.; Müller, D.; Althausen, D.; Wirth, M.; Fix, A.; et al. Depolarization ratio profiling at several wavelengths in pure Saharan dust during SAMUM 2006. *Tellus B Chem. Phys. Meteorol.* **2009**, *61*, 165–179. https://doi.org/10.1111/j.1600-0889.2008.00396.x.
12. Baars, H.; Seifert, P.; Engelmann, R.; Wandinger, U. Target categorization of aerosol and clouds by continuous multiwavelength-polarization lidar measurements. *Atmos. Meas. Tech.* **2017**, *10*, 3175–3201. https://doi.org/10.5194/amt-10-3175-2017.
13. Floutsi, A.A.; Baars, H.; Engelmann, R.; Althausen, D.; Ansmann, A.; Bohlmann, S.; Heese, B.; Hofer, J.; Kanitz, T.; Haarig, M.; et al. DeLiAn – a growing collection of depolarization ratio, lidar ratio and Ångström exponent for different aerosol types and mixtures from ground-based lidar observations. *Atmos. Meas. Tech.* **2023**, *16*, 2353–2379. https://doi.org/10.5194/amt-16-2353-2023.
14. Kai, K.; Nagata, Y.; Tsunematsu, N.; Matsumura, T.; Kim, H.S.; Matsumoto, T.; Hu, S.; Zhou, H.; Abo, M.; Nagai, T. The Structure of the Dust Layer over the Taklimakan Desert during the Dust Storm in April 2002 as Observed Using a Depolarization Lidar. *J. Meteorol. Soc. Jpn.* **2008**, *86*, 1–16. https://doi.org/10.2151/jmsj.86.1.
15. Zhang, S.; Huang, Z.; Li, M.; Shen, X.; Wang, Y.; Dong, Q.; Bi, J.; Zhang, J.; Li, W.; Li, Z.; et al. Vertical Structure of Dust Aerosols Observed by a Ground-Based Raman Lidar with Polarization Capabilities in the Center of the Taklimakan Desert. *Remote Sens.* **2022**, *14*, 2461. https://doi.org/10.3390/rs14102461.
16. Bi, J.; Li, Z.; Zuo, D.; Yang, F.; Li, B.; Ma, J.; Huang, Z.; He, Q. Dust Aerosol Vertical Profiles in the Hinterland of Taklimakan Desert During Summer 2019. *Front. Environ. Sci.* **2022**, *10*, 851915. https://doi.org/10.3389/fenvs.2022.851915.
17. Elshora, M.; Xia, H.; Su, L.; Wei, T. Observation and study of consecutive dust storms in the Taklimakan Desert from March 16 to 27, 2022, using reanalysis models and lidar. *Atmos. Res.* **2024**, *305*, 107431. https://doi.org/10.1016/j.atmosres.2024.107431.
18. Meng, L.; He, Q.; Zhao, T.; Zhang, H.; Yang, X.; Mamtimin, A.; Yang, F.; Zhou, C.; Huo, W. Interactions between dust aerosols and the ultra-high atmospheric boundary layer: Case study of vertical observation over the Taklimakan Desert, China. *Atmos. Environ.* **2025**, *343*, 120977. https://doi.org/10.1016/j.atmosenv.2024.120977.
19. Belegante, L.; Bravo-Aranda, J.A.; Freudenthaler, V.; Nicolae, D.; Nemuc, A.; Ene, D.; Alados-Arboledas, L.; Amodeo, A.; Pappalardo, G.; D'Amico, G.; et al. Experimental techniques for the calibration of lidar depolarization channels in EARLINET. *Atmos. Meas. Tech.* **2018**, *11*, 1119–1141. https://doi.org/10.5194/amt-11-1119-2018.
20. Kollias, P.; Clothiaux, E.E.; Miller, M.A.; Albrecht, B.A.; Stephens, G.L.; Ackerman, T.P. Millimeter-Wavelength Radars: New Frontier in Atmospheric Cloud and Precipitation Research. *Bull. Am. Meteorol. Soc.* **2007**, *88*, 1608–1624. https://doi.org/10.1175/BAMS-88-10-1608.
21. Myagkov, A.; Kneifel, S.; Rose, T. Evaluation of the reflectivity calibration of W-band radars based on observations in rain. *Atmos. Meas. Tech.* **2020**, *13*, 5799–5825. https://doi.org/10.5194/amt-13-5799-2020.
22. Wang, M.; Ming, H.; Huo, W.; Xu, H.; Li, J.; Li, X. Detecting sand-dust storms using a wind-profiling radar. *J. Arid Land* **2017**, *9*, 753–762. https://doi.org/10.1007/s40333-017-0031-5.
23. Wang, M.; Ming, H.; Ruan, Z.; Gao, L.; Yang, D. Quantitative detection of mass concentration of sand-dust storms via wind-profiling radar and analysis of Z–M relationship. *Theor. Appl. Climatol.* **2018**, *131*, 927–935. https://doi.org/10.1007/s00704-016-2012-6.

24. Ming, H.; Wei, M.; Wang, M. Quantitative Detection of Dust Storms with the Millimeter Wave Radar in the Taklimakan Desert. *Atmosphere* **2019**, *10*, 511. https://doi.org/10.3390/atmos10090511.
25. Ming, H.; Wang, M.; Zhang, J.; Wang, Y.; Gao, M. Study on the scattering characteristics of Ka millimeter wave by dust storms. *J. Quant. Spectrosc. Radiat. Transf.* **2022**, *277*, 107998. https://doi.org/10.1016/j.jqsrt.2021.107998.
26. Si, H.; Zhang, X.; Wang, M.; Ming, H.; Zhang, J.; Zhu, C. Dust-Storm detection analysis based on W-Band radar. *J. Electromagn. Waves Appl.* **2026**, *40*, 2560–2581. https://doi.org/10.1080/09205071.2026.2692485.
27. Madonna, F.; Amodeo, A.; D'Amico, G.; Mona, L.; Pappalardo, G. Observation of non-spherical ultragiant aerosol using a microwave radar. *Geophys. Res. Lett.* **2010**, *37*, L21814. https://doi.org/10.1029/2010GL044999.
28. Madonna, F.; Amodeo, A.; D'Amico, G.; Pappalardo, G. A study on the use of radar and lidar for characterizing ultragiant aerosol. *J. Geophys. Res. Atmos.* **2013**, *118*, 10056–10071. https://doi.org/10.1002/jgrd.50789.
29. Gumà-Claramunt, P.; Madonna, F.; Amodeo, A.; Bauer-Pfundstein, M.; Papagiannopoulos, N.; Rosoldi, M.; Pappalardo, G. Giant Aerosol Observations with Cloud Radar: Methodology and Effects. *Remote Sens.* **2025**, *17*, 419. https://doi.org/10.3390/rs17030419.
30. Gumà-Claramunt, P.; Amodeo, A.; Madonna, F.; Papagiannopoulos, N.; De Rosa, B.; Papanikolaou, C.A.; Rosoldi, M.; Pappalardo, G. Combined Raman Lidar and Ka-Band Radar Aerosol Observations. *Remote Sens.* **2025**, *17*, 2662. https://doi.org/10.3390/rs17152662.
31. Gao, X.; Xie, L. A scheme to detect the intensity of dusty weather by applying microwave radars and lidar. *Sci. Total Environ.* **2023**, *859*, 160248. https://doi.org/10.1016/j.scitotenv.2022.160248.
32. Irbah, A.; Delanoë, J.; van Zadelhoff, G.J.; Donovan, D.P.; Kollias, P.; Puigdomènech Treserras, B.; Mason, S.; Hogan, R.J.; Tatarevic, A. The classification of atmospheric hydrometeors and aerosols from the EarthCARE radar and lidar: The A-TC, C-TC and AC-TC products. *Atmos. Meas. Tech.* **2023**, *16*, 2795–2820. https://doi.org/10.5194/amt-16-2795-2023.
33. Mason, S.L.; Hogan, R.J.; Bozzo, A.; Pounder, N.L. A unified synergistic retrieval of clouds, aerosols, and precipitation from EarthCARE: The ACM-CAP product. *Atmos. Meas. Tech.* **2023**, *16*, 3459–3486. https://doi.org/10.5194/amt-16-3459-2023.
34. Luke, E.P.; Kollias, P.; Johnson, K.L.; Clothiaux, E.E. A Technique for the Automatic Detection of Insect Clutter in Cloud Radar Returns. *J. Atmos. Ocean. Technol.* **2008**, *25*, 1498–1513. https://doi.org/10.1175/2007JTECHA953.1.
35. Chandra, A.S.; Kollias, P.; Giangrande, S.E.; Klein, S.A. Long-Term Observations of the Convective Boundary Layer Using Insect Radar Returns at the SGP ARM Climate Research Facility. *J. Clim.* **2010**, *23*, 5699–5714. https://doi.org/10.1175/2010JCLI3395.1.
36. Drake, V.A.; Reynolds, D.R. *Radar Entomology: Observing Insect Flight and Migration*; CABI: Wallingford, UK, 2012. https://doi.org/10.1079/9781845935566.0000.
37. Williams, C.R.; Johnson, K.L.; Giangrande, S.E.; Hardin, J.C.; Öktem, R.; Romps, D.M. Identifying insects, clouds, and precipitation using vertically pointing polarimetric radar Doppler velocity spectra. *Atmos. Meas. Tech.* **2021**, *14*, 4425–4444. https://doi.org/10.5194/amt-14-4425-2021.
38. Yang, L.; Wang, Y.; Wang, Z.; Yang, Q.; Fan, X.; Tao, F.; Zhen, X.; Yang, Z. Automatic Identification of Clear-Air Echoes Based on Millimeter-wave Cloud Radar Measurements. *Adv. Atmos. Sci.* **2020**, *37*, 912–924. https://doi.org/10.1007/s00376-020-9270-z.
39. Hu, X.; Ge, J.; Du, J.; Li, Q.; Huang, J.; Fu, Q. A robust low-level cloud and clutter discrimination method for ground-based millimeter-wavelength cloud radar. *Atmos. Meas. Tech.* **2021**, *14*, 1743–1759. https://doi.org/10.5194/amt-14-1743-2021.
40. Grimm, H.; Eatough, D.J. Aerosol Measurement: The Use of Optical Light Scattering for the Determination of Particulate Size Distribution, and Particulate Mass, Including the Semi-Volatile Fraction. *J. Air Waste Manag. Assoc.* **2009**, *59*, 101–107. https://doi.org/10.3155/1047-3289.59.1.101.
41. Hersbach, H.; Bell, B.; Berrisford, P.; Hirahara, S.; Horányi, A.; Muñoz-Sabater, J.; Nicolas, J.; Peubey, C.; Radu, R.; Schepers, D.; et al. The ERA5 global reanalysis. *Q. J. R. Meteorol. Soc.* **2020**, *146*, 1999–2049. https://doi.org/10.1002/qj.3803.
42. NOAA National Centers for Environmental Information. *ETOPO 2022 15 Arc-Second Global Relief Model*; NOAA National Centers for Environmental Information: Asheville, NC, USA, 2022. https://doi.org/10.25921/fd45-gt74.
43. European Space Agency. *Copernicus DEM–Global and European Digital Elevation Model (GLO-30)*; European Space Agency: Paris, France, 2022. https://doi.org/10.5270/ESA-c5d3d65.
44. Probert-Jones, J.R. The radar equation in meteorology. *Q. J. R. Meteorol. Soc.* **1962**, *88*, 485–495. https://doi.org/10.1002/qj.49708837810.
45. Hinds, W.C. *Aerosol Technology: Properties, Behavior, and Measurement of Airborne Particles*, 2nd ed.; John Wiley & Sons: New York, NY, USA, 1999.
46. Wilks, D.S. Resampling Hypothesis Tests for Autocorrelated Fields. *J. Clim.* **1997**, *10*, 65–82. https://doi.org/10.1175/1520-0442(1997)010<0065:rhtfaf>2.0.co;2.
47. Balme, M.; Greeley, R. Dust Devils on Earth and Mars. *Rev. Geophys.* **2006**, *44*, RG3003. https://doi.org/10.1029/2005RG000188.
48. Wilson, J.W.; Weckwerth, T.M.; Vivekanandan, J.; Wakimoto, R.M.; Russell, R.W. Boundary Layer Clear-Air Radar Echoes: Origin of Echoes and Accuracy of Derived Winds. *J. Atmos. Ocean. Technol.* **1994**, *11*, 1184–1206. https://doi.org/10.1175/1520-0426(1994)011<1184:BLCARE>2.0.CO;2.

49. Doviak, R.J.; Zrnić, D.S. *Doppler Radar and Weather Observations*, 2nd ed.; Academic Press: San Diego, CA, USA, 1993.
50. Bohren, C.F.; Huffman, D.R. *Absorption and Scattering of Light by Small Particles*; John Wiley & Sons: New York, NY, USA, 1983. https://doi.org/10.1002/9783527618156.
51. Schimmel, W.; Kalesse-Los, H.; Maahn, M.; Vogl, T.; Foth, A.; Garfias, P.S.; Seifert, P. Identifying cloud droplets beyond lidar attenuation from vertically pointing cloud radar observations using artificial neural networks. *Atmos. Meas. Tech.* **2022**, *15*, 5343–5366. https://doi.org/10.5194/amt-15-5343-2022.

Disclaimer/Publisher's Note: The statements, opinions and data contained in all publications are solely those of the individual author(s) and contributor(s) and not of MDPI and/or the editor(s). MDPI and/or the editor(s) disclaim responsibility for any injury to people or property resulting from any ideas, methods, instructions or products referred to in the content.